AN ABSTRACT OF THE THESIS OF

Allyson K. Kitto for the degree of Master of Science in Nuclear Engineering presented on December 5, 2012.

Title: Determination of a Calculation Bias in the MCNP Model of the OSTR

Abstract approved:

Andrew C. Klein

Oregon State University is home to a TRIGA® Mark II reactor. In October of 2008, the reactor began operating on low enriched uranium fuel. A model of the facility exists in MCNP, a Monte Carlo code that can be used for criticality calculations. Until now, a bias in the calculation of the neutron multiplication factor has been carried forward from outdated core models.

This work involves updating various aspects of the model, including the geometry of the facility as well as materials and their properties, in order to arrive at a more accurate representation of the facility as it is today. The individual effect that each change has on the results of MCNP calculations of the core is documented.

Following the updates to the model, the model can emulate records that describe the startup of the reactor in October of 2008. The results of these calculations can be compared to actual data in order to establish a foundation for benchmarking the model and characterizing the reactor core. The deviation between calculated and expected results can be used to determine a single reactivity bias in the model.

The bias determined as a result of this work can be applied to future calculations using the model developed as a part of this work.

Determination of a Calculation Bias in the MCNP Model of the OSTR

by
Allyson K. Kitto

A THESIS

submitted to

Oregon State University

in partial fulfillment of
the requirements for the
degree of

Master of Science

Presented December 5, 2012
Commencement June 2013

Master of Science thesis of Allyson K. Kitto presented on December 5, 2012.

APPROVED:

Major Professor, representing Nuclear Engineering

Head of the Department of Nuclear Engineering and Radiation Health Physics

Dean of the Graduate School

I understand that my thesis will become part of the permanent collection of Oregon State University libraries. My signature below authorizes release of my thesis to any reader upon request.

Allyson K. Kitto, Author

ACKNOWLEDGEMENTS

I would like to thank Dr. Andrew Klein, my major professor, and Dr. Steven Reese, a co-advisor over the past few years. The combination of their enthusiasm for me to complete this work along with financial support throughout was the foundation by which it was possible for me to succeed. Thank you also to Todd Keller who was always available for technical support. All of the information and data I sifted through as well as all of the knowledge of the reactor and operations I needed in order to be successful, I gained through him. Combined these three helped guide me, readily allowing me to bounce questions off of them and eagerly awaiting the answers they left me to find.

Thank you also to all of my family, friends, and fellow students who saw me through this. Your tough love attitude was most motivating.

TABLE OF CONTENTS

TABLE OF CONTENTS (Continued)

LIST OF FIGURES

LIST OF TABLES

LIST OF ACRONYMS

Acronym	
30/20	30% uranium enriched to 20% ^{235}U
AFCR	Air Followed Control Rod
ARI	All Rods In
ARO	All Rods Out
β	Effective delayed neutron fraction
barn	10^{-24} cm^2
°C	degrees Celsius
cm	centimeter
cps	counts per second
CFR	Code of Federal Regulations
DRW	Differential Rod Worth
ENDF	Evaluated Nuclear Data File
FFCR	Fuel Followed Control Rod
FLIP	Fuel Life Improvement Program
g	gram
HEU	Highly Enriched Uranium
ICIT	In-Core Irradiation Tube
INL	Idaho National Laboratory
IRW	Integral Rod Worth
k_{eff}	Effective neutron multiplication factor
K	Kelvin
kW	Kilowatt
l	mean neutron lifetime
λ	decay constant
LANL	Los Alamos National Laboratory
LEU	Low Enriched Uranium
MCNP	Monte Carlo N-Particle
MWd	Megawatt day
NRAD	Neutron Radiography

LIST OF ACRONYMS (Continued)

NRC	Nuclear Regulatory Commission
OSU	Oregon State University
OSTR	Oregon State TRIGA® Reactor
ρ	Reactivity, in pcm
ρ_0	Reactivity, in dollars ($)
pcm	per cent mille
RERTR	Reduced Enrichment for Research and Test Reactors
RSICC	Radiation Safety Information Computational Center
σ	Standard Deviation
SAR	Safety Analysis Report
SDM	Shutdown Margin
TRIGA®	Training, Research, Isotope, General Atomics
μg	microgram
$^{w}/_{0}$	weight percent

LIST OF DEFINITIONS

Batch	Combination of parts of two fuel meats used to create fuel pellets
Cell	Fully enclosed, three-dimensional body defined in MCNP by the intersection of surfaces
Core Excess	The amount by which criticality is exceeded with all control rods fully withdrawn
Critical	A reactivity condition where the number of neutrons in a previous generation is the same as in the current generation; $k_{eff} = 1.0$
Element	Complete structure of fuel, in-core graphite reflector, or control rod, including inner material, cladding, and top and bottom fixtures
Meat	Initial mixture of fuel constituents
Shutdown	The amount by which reactivity is less than critical with all control rods fully inserted
Slug	Fuel pellet
Surface	A two-dimensional body defined assigned coordinates and orientation in space

1. Introduction

Oregon State University is home to a TRIGA® Mark II reactor (OSTR) manufactured by General Atomics[1]. Prior to August of 2008, the OSTR operated on highly enriched uranium (HEU) fuel. By October of 2008, HEU fuel was removed from the OSTR and replaced with low enriched uranium (LEU) fuel, in accordance with NRC regulation 10 CFR §50.64: Limitations on the use of HEU in domestic non-power reactors[2]. During and following the fuel conversion, startup testing was performed and documented, giving an excellent opportunity to benchmark and improve existing computer models of the reactor core.

1.1. Research Objective

The objective of this work is to update an existing MCNP model of the OSTR in order to provide a single value for the amount by which the model over-predicts or under-predicts the reactivity of the OSTR. This value will be presented as a reactivity bias. In the original form of the MCNP model, a large bias exists between the measured and actual reactivity of the core. Each change to the model has a quantifiable effect on the reactivity bias. Following implementation of each change to the model (made to improve accuracy and match as closely as possible the OSTR following the HEU to LEU fuel conversion), the model is used to mimic fuel configurations and measurements taken during startup testing. The difference between measurements taken during startup testing and calculations modeling the testing is used to quantify the reactivity discrepancy of the updated MCNP reactor model. The goal of the combined model changes and startup test comparisons is to arrive at a more accurate model. This will lead to more consistent and predictable variations between measured and calculated quantities in future calculations that use this model.

1.1.1. Scope

The scope of the changes made to the model includes:

- Addition of radial beam ports 1 and 2; as the model was received, only beam ports 3 and 4 were included, and the first change was to add the two missing beam ports.

- Water saturation of the radial graphite reflector; the graphite reflector was originally modeled with a pure carbon graphite composition, but it is updated here to reflect the suspected water saturation of the graphite as a result of the failure of the integrity of the aluminum jacket.
- Adjustment of fuel slug isotopic concentrations to reflect manufactured fuel measurements; each fuel element was originally modeled with a generic and uniform material composition, but the fuel slugs are updated here to reflect the actual material concentration in each fuel element.
- Inclusion of measured trace impurities in fuel mixtures; impurity concentrations were calculated for each fuel meat and incorporated into the material compositions.
- Modification of fuel element geometry to distinguish individual fuel slugs; the fuel element geometry was changed from five axial nodes to six axial nodes so that the geometry of each fuel slug can be exactly modeled by two axial nodes.
- Addition of estimated hafnium impurity in fuel mixtures; the hafnium concentration was measured for two different fuel meats and this weight percent was applied to each of the fuel slugs in the core.
- Use of various cross section data libraries; the MCNP model used ENDF cross section data that is no longer the most recently available, so the data was updated to the most recently available versions of ENDF data, with the exception of special consideration for zirconium, for which cross section libraries were explored in more detail.

The extent of the startup tests modeled for reactivity comparison includes:

- Approach to criticality; the continual loading of fuel elements until the reactor reaches a critical state.

- Core excess and shutdown margin; once a critical core is reached, the excess reactivity and available worth of the control rods is measured as the core continues to be loaded.
- Control rod worths; the differential and integral rod worths are measured by calculating the reactor period or changes in reactivity due to control rod movements.
- Critical rod heights; various control rod heights exist in which the core is exactly critical.

Measurements during startup testing were performed for many cold critical fuel configurations and control rod positions. Multiple calculations will be compared to measured test values.

1.1.2. Objective

The purpose of this work is to develop for use a more accurate MCNP model of the OSTR and determine the lowest achieved reactivity bias inherent in the final model. Within the bias determination, the magnitude of effect that individual considerations have on reactivity bias will be better understood and used for future model improvement or manipulation.

1.2. OSU TRIGA Background

The reactor at OSU is a TRIGA® Mark II General Atomics design. The core has 91 15-inch locations for fuel elements, in-core irradiation facilities, one void-followed control rod, and three fuel-followed control rods, surrounded by a ring of 36 graphite reflector elements. As the void-followed control rod is withdrawn from the core, absorber volume is replaced by void coming up from below the core. A fully withdrawn void-followed rod will completely replace absorbing material with air. As the fuel-followed control rods are withdrawn from the core, absorber volume is replaced by fuel elements coming up from below the core. A fully withdrawn fuel-followed rod will completely replace absorbing material with fuel elements. It is a pool-type reactor with steady-state operation up

to 1.1 MW of thermal power. When operated in pulse mode, the OSTR can reach instantaneous power levels of 3,200 MW[3].

Multiple irradiation facilities exist around the reactor. The lazy Susan located directly surrounding the core has numerous evenly spaced locations where samples can be placed. The lazy Susan can be rotated around the core to ensure consistent irradiation of samples. The in-core irradiation tube (ICIT), as well as the cadmium-lined ICIT and G-ring ICIT are irradiation facilities located in the core for sample irradiation. The ICIT is located in the B-1 position near the center of the core. Similar to the ICIT, the cadmium-lined facility (CLICIT) is an aluminum tube with an additional layer of cadmium. The G-ring facility is located in the outermost ring made of graphite reflectors and experiences a smaller flux than the ICIT and CLICIT. Outside of the core are a tangential beam port and 3 radial beam ports. The radial beam ports are aimed directly into the core and so have greater flux than the tangentially aligned beam port.

1.3. LEU Conversion

Although the facility would not require any changes, in the early 2000s steps were underway to comply with NRC regulation and convert the TRIGA® fuel from HEU to LEU.

1.3.1. Previous HEU Core

Prior to the conversion to LEU fuel, the OSTR operated with HEU FLIP (Fuel Life Improvement Program) fuel encompassed in a ring of aluminum-clad graphite reflectors. HEU FLIP fuel is a mixture of uranium, erbium, hydrogen, and zirconium, where the mixture is 8.5% uranium by mass and the uranium is enriched to 70% ^{235}U by mass. Major advantages of the HEU fuel are the high neutron fluxes seen by the irradiation facilities and the much longer expected lifetime due to the higher burnup that can be achieved through higher enrichment. The estimated HEU FLIP fuel lifetime is approximately 3,800 MWd[1].

In 1986 the NRC introduced 10 CFR §50.64, a new regulation requiring non-power reactors to develop and implement a proposal for replacing HEU fuel with LEU fuel[2]. The conversion at OSU was completed and criticality of the LEU core was achieved in October of 2008[4].

1.3.2. Modifications to OSTR from Conversion

At the time of conversion a ring of aluminum-clad graphite reflector elements surrounding the core was also removed. The graphite elements were replaced by new graphite reflectors clad with stainless steel. Stainless steel clad was also replaced on the four control rods. The new LEU fuel that was installed remains a mixture of uranium, erbium, hydrogen, and zirconium, but with a mixture that is 30% uranium by mass and 19.75% enriched ^{235}U[1]. Neutronic calculations of core performance with 30/20 LEU fuel versus HEU FLIP fuel were carried out in order to determine the appropriate fraction of erbium required to demonstrate adequate core performance while not sacrificing the benefits of HEU fuel[5]. To this end, 1.1% erbium (rather than a more common 0.9% erbium) proved to enhance the safety of the fuel by making the fuel temperature coefficient more negative, allowing for a larger critical core size[5], and maintaining a comparable fuel lifetime of approximately 3,600 MWd[1].

1.4. Reactor Model

An existing Monte Carlo N-Particle (MCNP) model of the OSTR is the basis for the changes and updates applied in this work. This tool will then be used to perform various comparisons between measured OSTR values and values calculated by the reactor model in an effort to reduce model error and determine a bias.

2. Literature Review

2.1. OSTR Post-Conversion Core Description

The OSTR maintains its original design and mechanical configurations. The conversion from HEU to LEU impacted only the elements positioned in the rings of the reactor core. In the central rings the fuel was converted from HEU FLIP fuel to LEU 30/20 fuel. All fuel element dimensions and mechanical structures remain essentially unchanged. In the outer ring, the aluminum-clad graphite reflector elements were replaced by stainless steel-clad reflector elements.

The components in the core of the OSTR include 86 full-length fuel elements, one AFCR, three FFCR, one source, and up to 36 reflector elements. A fuel element is illustrated in Figure 2-1.

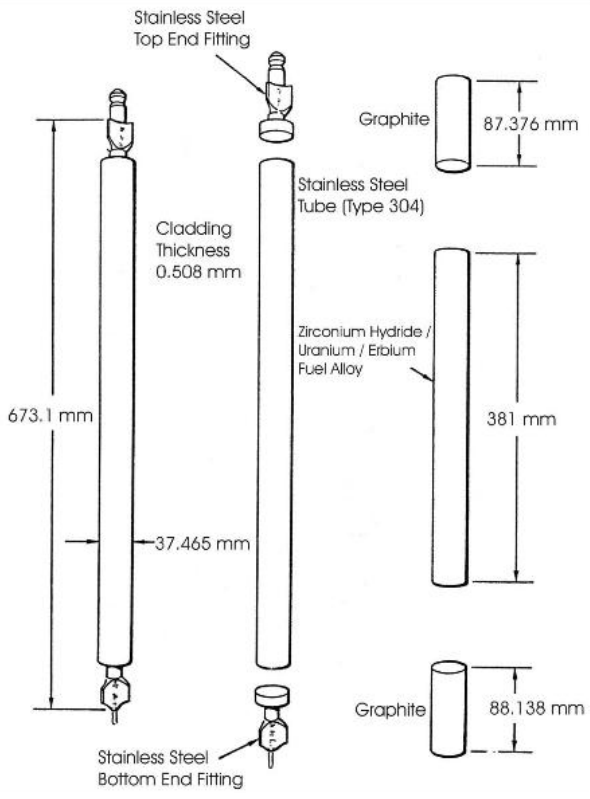

Figure 2-1. Fuel element illustration.

The placement of the fuel elements, control rods, graphite reflector elements, and in-core irradiation facilities can be seen in Figure 2-2. The core is

laid out in rings that extend radially outward from a central location. There are six rings for fuel element, control rod, and ICIT locations. The outermost ring is reserved for graphite reflector elements, the neutron source, and GRICIT.

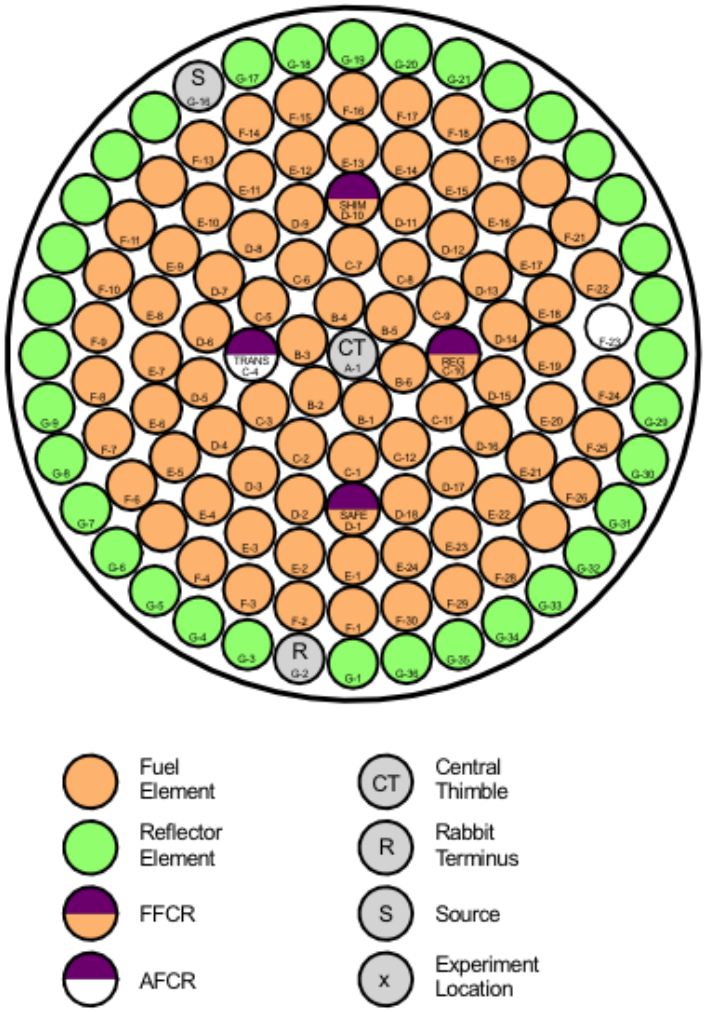

Figure 2-2. Core element configuration.

2.2. Prior HEU-LEU Fuel Conversions

The original TRIGA designs utilized the HEU FLIP fuel for high neutron flux and infrequent refueling made possible by higher achievable burnup. Research and test reactors that were previously permitted to operate on HEU fuel are now required to convert their cores to operate using LEU fuel. TRIGA reactors that

have undergone the HEU to LEU conversion are listed in Table 2-1, including the reactor type, steady-state power level, and date of conversion, if any occurred.

Table 2-1. TRIGA test and research reactors.

Facility[6]	Reactor Type[6]	Power (kW) [6]	Conversion
Cornell University	TRIGA Mark II	500	
Kansas State University	TRIGA Mark II	250	
U. C. Davis Nuclear Radiation Center	TRIGA Mark II	2000	
Oregon State University	TRIGA Mark II	1100	October 2008
Pennsylvania State University	TRIGA Conversion Mark III	1000	
Reed College	TRIGA Mark I	250	
Texas A&M University	TRIGA Conversion (TRIGA Mark I)	1000	August 2006
University of California – Irvine	TRIGA Mark I	250	
University of Maryland	TRIGA	250	
University of Texas – Austin	TRIGA Mark II	1100	
University of Utah	TRIGA Mark I	100	
University of Wisconsin	TRIGA Conversion	1000	September 2009
U.S. Geological Survey	TRIGA Mark I	1000	
U.S. Veterans Administration	TRIGA Mark I	20	
Washington State University	TRIGA Conversion	1000	October 2008
Idaho National Lab (ANL – West)	NRAD TRIGA Mark II	250	March 2010

2.2.1. Benchmarking

The MCNP model of the OSTR will be updated to give a more accurate representation of the actual facility geometry and materials. Next the model will be used to test perturbations to sensitive or unknown parameters, explore possible shortcomings in the computational tools used, and finally the magnitude of the impact that each of these considerations has on the calculated k_{eff} of the core model will be determined.

Upon completion of the fuel conversion and prior to normal use of the reactor, startup testing was performed. This testing was done to support the safety analysis of the reactor, inform operators of the total and differential worth of the control rods, determine the excess reactivity in the core, and calculate the available shutdown margin.

Once the core model was updated to reflect the highest known accuracy of the materials and configurations of the facility, the model was used to calculate k_{eff} for many of the configurations used during startup testing. These calculated values were compared against the measured values in order to determine a general precedent for the difference in actual and calculated reactivity. A sufficiently thorough comparison of calculated and measured values is expected to establish a consistent difference in results. Any consistent trend in the results can be averaged and used as the effective reactivity bias of the model.

2.2.2. Neutron Radiography Facility

The Neutron Radiography (NRAD) facility at the Idaho National Laboratory (INL) is a TRIGA® Mark II research reactor. The NRAD facility is similar to the OSTR in that it is a pool-type reactor with two beam ports, graphite reflectors, and 15” high fuel elements of similar mechanical design. The NRAD fuel elements are arranged in four-element assemblies in a square lattice, controlled by three water-followed control rods. When the NRAD first began operation it was loaded with the same HEU FLIP fuel that the OSTR had

utilized. In response to the Reduced Enrichment for Test and Research Reactor (RERTR) Program, the HEU FLIP fuel was removed and replaced with LEU (30/20) fuel. This LEU fuel is 30% by weight uranium enriched to 20% ^{235}U and 0.9% natural erbium burnable poison and clad in stainless steel.

2.2.2.1. NRAD Benchmarking

Following the conversion to LEU fuel in the TRIGA® at the NRAD facility at INL, benchmarking analysis was used to characterize the geometry and material changes resulting from the conversion, evaluate sub-critical and critical core configurations, and examine the impact that different cross section data and variation in material composition had on results[7].

Many of the sources of inaccuracies that were expected in the MCNP model of the NRAD facility are also anticipated to affect the accuracy of the MCNP model of the OSTR. Similar parameters addressed are the cross section libraries, both on an elemental and core-wide basis, and the water saturation of the graphite reflector block[7].

2.2.3. Evaluated Resources

Calculations in support of this work rely on cross section data included in the MCNP code package. The most recent cross section library, which is of primary use for most of the materials in the model, is the ENDF/B-VII cross section library. The cross sections for this version of the ENDF library are available at 293 K and 600 K[8]. For most calculations, materials will be referenced at the lower temperature of 293 K to match more closely the conditions of the low power startup testing[9].

2.2.3.1. Nuclear Data Libraries

The most recently released neutron data library maintained for use with the MCNP code package is ENDF/B-VII.0. In order to accurately capture every material in the TRIGA® LEU fuel, 96 isotopes or naturally occurring element cross sections are used. Dozens of impurities were

measured in the fuel, and because this information is known, it can be modeled. The only isotope unavailable to include in the fuel makeup is ^{180}W, which makes up 0.12% of all tungsten[10], and only appears in trace amounts in the fuel. Although this is the most recent release of an ENDF cross section library and has nearly all isotopes available, there is no guarantee that neutron cross sections will be modeled better with the current version of this data library than with any other version or library.

Calculations were performed during the LEU conversion of the NRAD facility in efforts to benchmark an MCNP model of the facility, and multiple cross section libraries and versions were considered. There did not seem to be a strong impact on the results, however, when considering a complete change from one library to another[11].

An additional consideration is for local inaccuracies in cross section data. This work went on to demonstrate that perhaps only certain elements need be considered in different libraries or versions. It was established that zirconium cross sections in ENDF/B-VII may be less accurate than previous versions. When using ENDF/B-VI, core calculations of the NRAD facility showed results closer to predicted outcomes than with ENDF/B-VII[11]. Because zirconium is in the fuel of both the NRAD and OSTR facilities, improper treatment of this material can lead to very erroneous results. While this possibility was explored primarily for zirconium, it is possible that this phenomenon exists for other materials as well.

2.2.3.2. Elemental Considerations

The results of calculations performed with MCNP are largely influenced by the nuclear data included in the model. It is expected that the most recent revisions to a nuclear data library have the most accurate or developed data, however, on an elemental basis, this may not be the case. The improvement of some elements with the change from ENDF/B-VI to

ENDF/B-VII may be called into question, as may the accuracy of using ENDF data in contrast to JEFF-3.1 or JENDL-3.3, for example.

Elemental erbium is included in the LEU fuel composition. Erbium acts as a burnable neutron poison that controls the burnup of the fuel and aids in lengthening the core life. Erbium also allows for a larger core because it lowers the overall reactivity of the fuel and results in the requirement that more fuel elements are needed to form a critical configuration. Erbium also causes a more negative prompt temperature reactivity coefficient[5], which is beneficial to the operation of the reactor.

At 1.1 wt% erbium in the fuel[5], the combination of close proximity to the most reactive part of the reactor model (the fuel lattice) and large negative impact on overall reactivity make accurate modeling of the both the isotopic content and cross sections crucial to producing dependable results. Small errors in this portion of the model have the potential to produce more impactful errors than something more removed, such as beam port geometry.

2.2.4. Computational Tools

A model of the OSTR has been constructed in three dimensions and is compatible with the MCNP5 v1.60 code system[12] developed at Los Alamos National Laboratory (LANL) and maintained by RSICC that uses a stochastic Monte Carlo approach to solve criticality and particle transport problems. An artifact of this stochastic approach is the availability of the standard error of the calculation and other forms of measuring the statistical fidelity of the calculation. Here, MCNP will be used to examine the criticality of the system; the most significant result will be the effective neutron multiplication factor, k_{eff}, and the associated standard deviation.

An MCNP model is a construct of surfaces, cells, and materials. Surfaces are defined generally in two dimensions. When surfaces intersect to form a fully enclosed three-dimensional body, that body can be defined as a

cell. Cells are then assigned materials that are compositions of one or more isotopes or elements.

2.2.5. Statistical Uncertainty

Because MCNP stochastically solves reactor criticality problems, a by-product of the solution is a set of information that quantifies the statistical uncertainty associated with the result. While the confidence of the Monte Carlo solution is presented in a variety of formats, the value with the greatest importance in the calculations to follow will be the standard deviation of the solution. One, two, and three standard deviations on either side of a mean represent 68%, 95%, and 99% confidence intervals in solution[12]. Anywhere a value for k_{eff} is reported as a result of an MCNP calculation, the standard deviation associated with that result will also be reported.

2.2.6. Computational Limitations

The fidelity of the results of the calculation when using MCNP is dictated by the number of particles included in a simulation history and the total number of histories included in the calculation. Generally speaking, there is a correlation between the number of particles and histories in the model and the improvement in the reported error of the calculation. Increasing the number of particles and histories used in the calculation will result in a roughly linear increase in computational time. However, reducing the standard error by a given factor would require an increase by the square of that factor in computational time. The tradeoff between precision and computational cost must be considered because of this. The magnitude of the error should be significantly smaller than the differential changes in the results of each calculation in order for each of the calculations to bear significance.

As is true with other computational tools for solving criticality or neutron transport problems, the user is largely limited by the cross section data available. Neutron libraries can have different data by way of cross sections associated with discrete energies, isotopic composition of natural elements, and

missing isotopes. Incomplete or inaccurate data will have impact on a calculation in the same way that selection of these different data sets may impact calculations.

2.2.7. Modeling Limitations

While the MCNP model was built as accurately as possible based on available information, there is a point at which a greater level of detail in the model will not yield equally better results. For example, every fuel slug is modeled with the same height and diameter, although in reality each has slightly different dimensions. The actual dimensions of the fuel slugs are known so the isotopic concentrations are accurately represented, but they are applied to a standard fuel slug shape. While the cumulative result of this estimation may have cancelling effects, on a finer level this detail may prove important.

In contrast to the simplification of some aspects of the model affecting the accuracy of the results, carrying forward too much detail may have the same effect. The concentrations of isotopes in the fuel are known to a reasonable degree, as well as a large number of impurities. Each of these measurements is associated with an uncertainty. Carrying forward too many significant digits in the determination of concentrations for each material can cause the calculation to be burdened by details. The potential computational limitations may not be made up for with greater accuracy or precision.

An appropriate level of detail for geometry, materials, and perturbations will help alleviate limitations to the accuracy or fidelity of the calculation.

2.3. Water Saturation of Graphite

Graphite is known to readily absorb water. The graphite block reflector that surrounds the core has been fully submerged in the reactor tank for the life of the reactor. Initially the graphite reflector was sealed in an aluminum jacket, however, it is suspected that the aluminum barrier has failed and water has been in direct contact with the reflector. It is expected that this graphite is well-saturated with

water and has different reactivity impact on the core than when the reflector was free of water. Water is well-suited for scattering and thermalizing neutrons in the core of the reactor and graphite is used to scatter and redirect neutrons back toward the core of the reactor, both materials promoting reactivity in thermal systems. Alone, the graphite reflector reduces neutron leakage and increases reactivity. However, the addition of water to the composition of the graphite reflector may not add positive reactivity. The volume of the graphite reflector has maintained fixed, however, the density may have increased with the addition of water molecules into interstitial vacancies and the naturally large open volumes in the carbon lattice of graphite[14]. The higher density of this region will result in more scattering and moderation of neutrons, and many more will lose too much energy to re-enter the core than otherwise would with a reflector composed solely of graphite.

The exact properties of the water-saturated reflector cannot be known without comparing as-built data to measurements taken following the removal of the reflector from the pool. Work supporting the HEU to LEU conversion of the NRAD Reactor at INL suggests one method for determining the composition based on the decrement between the actual density of the graphite at the time it was placed in the core and theoretical density[7].

The density of the graphite reflector at the NRAD facility is given as 1.57 g/cm^3 and the theoretical density of graphite is 2.25 g/cm^3. Dividing the actual density by the theoretical density will give the fraction that the graphite density is of the theoretical density (approximately 70%). It is suggested then that the remaining 30% of the theoretical density not accounted for could be made up instead by the water surrounding and saturating the graphite.

A review of the literature suggests that this is not a fully sufficient determination of the water composition in graphite. Not only can the water molecules occupy the vacancies of the carbon lattice associated with the less-than-theoretical density of the material, but water molecules can also exist

within a carbon lattice of full theoretical density because water molecules are sufficiently smaller than the lattice spacing of the graphite that the molecules can fit within, even accounting for inter-molecular interactions[13] [14].

3. Materials and Methods

The efforts to update the OSTR model and perform an analysis of various components of the model were a multi-step process. A calculation of the effective neutron multiplication factor for the MCNP model in its original form was performed to define a starting point to benchmark the macroscopic effect of each modification. The approach of making a single modification at a time allows the impact of each parameter to be quantified individually.

Each change to the model is informed by a combination of different sources of information and calculations. A collection of reactor documentation and data was used as the basis for the known, physical modifications to the model. Facility blueprints maintained in the reactor building were used to provide measurements of the beam port geometry. Documentation accompanying the delivery of the LEU fuel is the source of all isotopic compositions in the fuel, traces of impurities, and physical specifications. The reactor startup log describes the placement and rearrangement of the fuel element and control rod locations during startup testing. The method of use of each of these materials will be discussed sequentially. Each calculation is based on the completed changes to the model from the prior case.

3.1. Facility Geometry

The OSTR facility is comprised of four beam ports, thus requiring the addition of two omitted beam ports to the MCNP model. The beam port geometry was determined from scaled blueprints of the facility. Each of the beam ports, as well as the interface between the beam ports and the various linings (water, aluminum, lead) of the reactor core can be seen from a top-down view of the facility in Figure 3-1. The top-to-bottom and side-to-side distances are measured from the geometric center of the core to where the outer circumferences of the beam ports interface with the reactor linings. With the combination of these distances and the measured diameters of each of the beam ports, the angle of orientation seen in Figure 3-1 that each beam port has to the reactor core is

determined. The angles between the beam port centerlines can also be determined using these measurements.

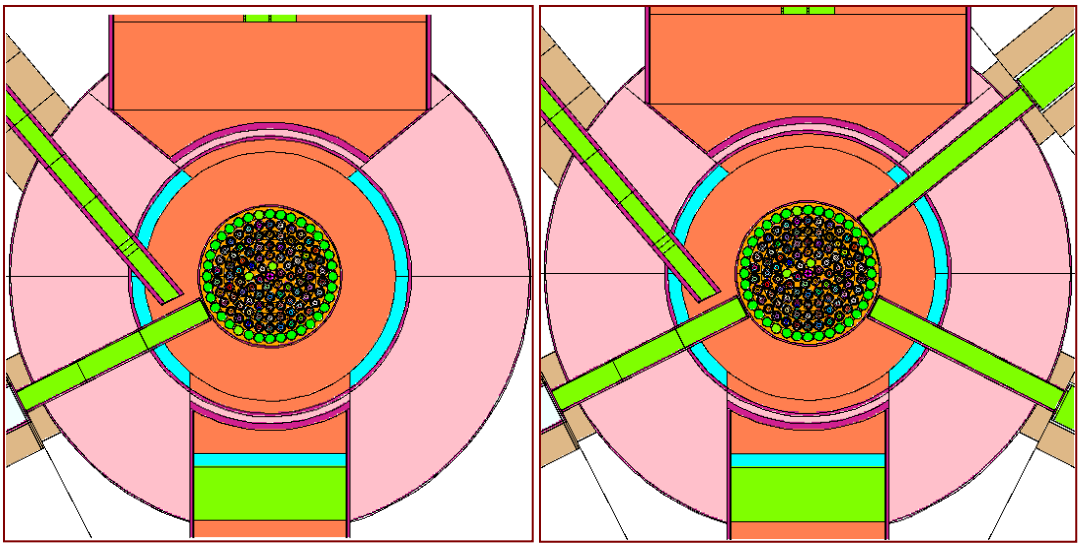

Figure 3-1. Model before and after addition of BP #1 and 2 (bottom up view).

Two beam ports were already included in the MCNP model; specifically the tangential beam port and one of the radially inward facing beam ports. Measurements taken of the beam port dimensions confirmed that the two radially inward facing beam ports excluded from the MCNP model have the same diameters and tube thicknesses as the one which had been included in the MCNP model. Measurements from the facility drawings agree with dimensions and orientation of the beam ports already in the model.

Surface and cell cards for the missing radial beam ports were developed using similar construction as the first radial beam port in the model. The missing beam ports were rotated to the appropriate orientation about the core with the use of the transpose data card. Using this card, a new set of x- and y-axes was defined for each beam port; the z-axis was not adjusted because the beam ports lie in the horizontal plane in which the model was constructed. The cells in which the newly added beam port cells pass through were updated to exclude the newly defined volumes. Each beam port was added individually in this manner, and a new k_{eff}

calculated each time. This allows the clear quantification of the effect a single beam port has.

3.2. Graphite Reflector Saturation

Following the implementation of accurate beam port geometry, the radial graphite reflector was considered. Because the reflector is still in the tank, the exact material composition is not known. However, it is largely assumed to be saturated with water because it has been submerged in the reactor pool since it was installed, and the aluminum casing installed around the reflector is assumed to have failed over the course of OSTR operation. The amount of water cannot be estimated with certainty by calculation, so numerous calculations for k_{eff} are performed over a range of saturation limits to attempt to gain a better understanding of the uncertainties associated with reflector saturation.

At the time of construction of the OSTR, as-built data was known for the reflector. The density is given as 1.698 g/cm^3 (a conversion from 0.085205 atoms/barn-cm, given in the MCNP model). Water is added to the graphite assuming the graphite has not been altered since initially being placed in the core, such as by fracturing or chipping, or by swelling. The result of adding water to the reflector will then effectively result in a change to the elemental composition and density of the reflector.

A separate material is created and assigned to the cell designated as the radial reflector. The composition and density can be changed on this card to account for varying reflector composition. The initial composition is given as 100% carbon (^{12}C) and the density (given as atom density) is 0.085205 $^{atoms}/_{barn\text{-}cm}$. Water saturation is considered in 5 $^{at}/_{0}$ increments. The fraction of each isotope in the saturated reflector is determined by:

$$C_{atom\ fraction} = \frac{100\% - Saturation\ \%}{100\%}$$

$$O_{atom\ fraction} = \frac{\frac{1}{3}(Saturation\ \%)}{100\%}$$

$$H_{atom\ fraction} = \frac{\frac{2}{3}(Saturation\ \%)}{100\%}$$

The composition of each isotope will be normalized (to avoid rounding errors in the input, the relative amounts of each isotope does not need to sum to unity). Once the atom fractions of each isotope are known, the calculation of the atom density is given by

$$100\%\ C\ atoms + \frac{Saturation\ \%}{100\%\ C\ atoms} = \%\ total\ atoms$$

$$\%\ total\ atoms \times original\ atom\ density\left(\frac{atoms}{barn-cm}\right) = new\ atom\ density\left(\frac{atoms}{barn-cm}\right)$$

As discussed previously, the theoretical density of graphite is roughly 2.25 g/cm^3 but the actual density for the as-built reflector is 1.698 g/cm^3. Because the graphite in the OSTR can become roughly 30% more dense, the preliminary assumption is made that the 30% density deficit can instead be made up by water.

3.3. Fuel Data

A public nuclear corporation, AREVA, manufactured the LEU fuel for the OSTR conversion. A report received with the delivery of the fuel documents detailed the conformance of the manufacturing to technical specifications, inspections, and test operations.

The fuel was made in eight different meats, meaning simply eight distinct mixtures of the requested concentrations of each element in the fuel composition. Chemical analysis was performed on each meat to determine the concentration of various detectable impurities. Batches of fuel were created out of 50/50 combinations of each of the different fuel meats, and the isotopic compositions for every fuel batch is given. Fuel slugs are created from the batch mixtures, and each fuel element is made of three fuel slugs. Slugs of the same batch are not often loaded into the same fuel element. Instead, the different batches are assigned positions throughout the fuel elements in order to more uniformly distribute the erbium.

Every fuel slug in the core is given a different material identification number in MCNP. Each fuel slug defined in MCNP is defined by the isotopes which comprise it, the atomic density of the isotope, and the data library to be used to assign cross section data to the isotope. When the material is assigned to a cell, the overall material density is provided.

Physical characteristics are given for every fuel slug, the slug location in every fuel element is given, and where applicable the tolerance on the measurement of this data is stated. A well-defined and detailed model of the fuel can be constructed entirely from this documentation. Once the as-built fuel is incorporated with sufficient detail, another calculation of k_{eff} can be performed to quantify the effect that moving from a generic core-wide fuel composition with limited detail to the as-built fuel has on the reactivity of the system.

3.3.1. Fuel Geometry

With the provided dimensions of each slug, the volume can be determined, and combined with the total mass, the individual density of each fuel element can be obtained.

$$Slug\ Volume\left(cm^3\right) = Length\ \left(cm\right) \times \pi \times \left(\frac{Outer\ Diameter\ \left(cm\right)}{2}\right)^2 - \left(\frac{Inner\ Diameter\ \left(cm\right)}{2}\right)^2$$

$$Slug\ Density\left(\frac{g}{cm^3}\right) = \frac{Mass\ \left(g\right)}{Slug\ Volume\ \left(cm^3\right)}$$

This information is determined for every slug, then used for converting raw composition data to unique atomic densities in each slug.

3.3.2. Fuel Composition

The fuel is a mixture of uranium enriched with ^{235}U, natural erbium, hydrogen, and zirconium. For each fuel slug, documentation provides the total mass of the slug, the mass and weight percent of the uranium, ^{235}U, erbium, and trace amounts of carbon, as well as the H/Zr atomic ratio. The uranium is assumed to consist only of ^{235}U and ^{238}U (other uranium isotopes will be considered impurities and are measured elsewhere). Based on this data and

assumption, the weight and weight percent of each of the isotopes in the fuel is known.

$$M_{H/Zr} = M_{Fuel} - M_U - M_{Er} - M_C$$

$$H\ wt\% = \frac{H/Zr\ ratio \times amu\ H}{H/Zr\ ratio \times amu\ H + amu\ Zr} \times (H + Zr)\ wt\%$$

$$Zr\ wt\% = \frac{amu\ \mathrm{Zr}}{H/Zr\ ratio \times amu\ H + amu\ Zr} \times (H + Zr)\ wt\%$$

The atomic densities for the major fuel constituents of which the fuel is made can be calculated by

$$Atomic\ Density\left(\frac{atoms}{barn-cm}\right) = \frac{\frac{wt\%_{isotope}}{100\%} \times Mass\ Fuel\ (g) \times \frac{6.022 \times 10^{23}\ atoms}{mol} \times \frac{10^{-24}\ cm^2}{barn}}{Molar\ Mass\left(\frac{g}{mol}\right) \times Volume\ (cm^3)}$$

For elements that appear as naturally occurring in the cross section library used in the calculation, this will be the final format of the atomic density. For elements that appear only as individual isotopes in the library, the relative abundance of each isotope as it appears in the 16th edition of the Chart of the Nuclides[10] is used to determine what fraction of the total atomic density is allotted to each isotope of the element in question.

3.3.3. Impurity Concentrations

A chemical analysis was performed for each fuel meat to measure the concentrations of various trace isotopes. The impurities from each fuel meat are combined for the fuel batches by taking the appropriate ratio of fuel meats in each batch. Then, using the atomic mass and calculated impurity concentration, the atomic densities for each of these detectable elements are determined.

$$Atomic\ Density\left(\frac{atoms}{barn-cm}\right) = \frac{Conc_{isotope} \times Mass\ Fuel\ (g) \times \frac{6.022 \times 10^{23}\ atoms}{mol} \times \frac{10^{-24}\ cm^2}{barn}}{Molar\ Mass\left(\frac{g}{mol}\right) \times Volume\ (cm^3)}$$

For elements that appear as naturally occurring in the cross section library used in the calculation, this will be the final format of the atomic

density. For elements that appear only as individual isotopes in the library, the relative abundance of each isotope as it appears in the 16th edition of the Chart of the Nuclides[10] is used to determine what fraction of the total atomic density is allotted to each isotope of the element in question.

3.3.4. Hafnium Content

The concentration of hafnium is not known for every fuel batch. Instead, analyses were performed for two reference fuel slugs from the same batch. The results of the analyses show the fuel slugs, by weight, have 7 or 8 μg of Hf per g of fuel with a 10% measurement uncertainty. A simple average of these numbers is taken (7.5×10^{-6} $w/_0$), and this weight percent is assumed for every fuel slug. The atomic density of hafnium in each fuel slug is then determined by

$$Atomic\ Density_{Hf}\left(\frac{atoms}{barn-cm}\right)=\frac{\frac{wt\%_{Hf}}{100\%}\times Mass\ Fuel\ (g)\times\frac{6.022\times10^{23}\,atoms}{mol}\times\frac{10^{-24}\,cm^2}{barn}}{Molar\ Mass_{Hf}\left(\frac{g}{mol}\right)\times Volume\ Fuel\ \left(cm^3\right)}$$

Because so much uncertainty exists surrounding the amount of hafnium in the fuel elements, perturbations were performed on the weight percent of hafnium to test the potential sensitivity to inaccurate representation. The weight percent of hafnium is varied from 5.0×10^{-6} $w/_0$ to 10.0×10^{-6} $w/_0$ in 0.5×10^{-6} $w/_0$ increments. The resulting k_{eff} for each of these perturbations is calculated, and the results can be used to determine the significance of the impact any uncertainty in the hafnium concentration has on the results.

In calculating the accepted amount of hafnium in the as-built fuel, the weight percent was used in combination with the fuel density to determine the unique atom density in each fuel slug. Conversely, for the cases of perturbed hafnium concentrations considered here, a uniform atom density for hafnium is determined based on an averaged fuel density, and this uniform atom density is then applied to every fuel slug.

3.3.5. Nuclear Data Library

The nuclear data cross section library used to perform calculations is the ENDF/B-VII.0 library at 293.6 K, which equates to 20°C. The measurements considered for comparison to this MCNP model all occur during low power testing of the OSTR during startup. Because the fuel has not yet been taken to any significant power level, the fuel and core will remain at ambient conditions, being the conditions of the reactor pool at standard pressure and room temperature. No significant amount of heat is created in the fuel or released to the surroundings, so performing calculations with this set of cross section data is reasonable.

The reactivity bias in the model is expected to have a certain sensitivity to the cross section data used for zirconium. This element is given a relative amount and assigned a cross section library on each material card for all of the fuel elements. Additionally, zirconium is defined on the "mt" cards corresponding to each of the fuel element material cards. There is additional cross section data defined for "zirconium in hydrogen" and "hydrogen in zirconium" that allows various nuclear data to be used. A variety of combinations of libraries for the different isotopes of zirconium and hydrogen were explored. The effective changes in reactivity from each permutation can characterize in part the contribution that the zirconium cross section data has on the overall reactivity bias of the model.

A critical configuration was used as the basis for comparing different cross section data.

3.4. Startup Logs

Following the implementation of the physical modifications, the MCNP model reflects the facility geometry and fuel element material compositions commensurate with the original loading of the LEU fuel and initiation of startup testing. Startup logs of these activities log the transfer of new reflector elements to the G-ring of the core and the placement of the four control rods. Each fuel

maneuver is accompanied with subcritical count rates or critical control rod heights and power level. The log follows:

1. The loading of reflector elements, control rods, and fuel elements into the core up through the achievement of a critical configuration
2. The continued addition of remaining fuel elements and associated critical rod heights at low power
3. Low power measurement of the integral rod worth (IRW) for each control rod
4. Partial power and full power operation and measurement of IRW, core excess, and shutdown margin (SDM).

3.4.1. Control Rod Position

Each of the four control rods is assigned a permanent location in the core. As they are withdrawn, three of the control rods are followed by LEU fuel elements of the same design and composition as the standard fuel elements. The other control rod is followed by air as it withdrawn. Once the new graphite reflectors are installed in the G-ring, the control rods are placed in the C- and D-rings. They are initially loaded in the all rods out (ARO) position, so effectively there are four locations in the core already loaded; three locations with fuel-followers, and one location filled with air.

Each of the control rods is defined in MCNP by a set of cells made by the intersection of surfaces. The location (height) of the control rods is adjusted by modifying the surfaces of the control rods that have an axial component. Axially the control rods span a 15-inch range from all rods in (ARI) to ARO, and throughout startup testing the control rods will be withdrawn to varying levels between 0 and 100%. The amount withdrawn will be controlled by modifying the control rod surfaces in the MCNP model.

3.4.2. Fuel Element Arrangement

With the control rods in the ARI position, new LEU fuel elements are loaded into the core. The rods are then pulled out to measure the count rate

while subcritical. Each fuel element has varying concentrations of each of its major constituents. They are assigned locations around the core such that a desired distribution of erbium can be achieved. Fuel elements with low erbium levels were loaded into the center of the core and high erbium levels loaded on the periphery. This causes slightly more elevated power levels in the center of the core, and the reactor can achieve criticality with fewer fuel elements. To a degree, this will help ensure symmetry in the power profile of the core. Each position in the core will only contain its assigned fuel element, or each cell defining the fuel or graphite element location will be filled with water.

While the core has few enough fuel elements loaded into it that it remains subcritical, the control rods remain out and multiple elements can be loaded at a time. Increasing count rates will indicate the core is nearing criticality and fuel elements will be loaded in smaller groups, then individually. Once the core has achieved a critical configuration fuel elements will continue to be loaded into the core with ARI, and for critical measurements the core will be at low power levels and the control rods will be partially inserted.

3.4.3. Approach to Critical

The core is initially modeled with only the control rods in the ARO position. With only 3 fuel elements loaded the core is amply subcritical. Subsequently, the B-ring and C-ring are filled with their respective fuel elements. Following the fill of each of these locations, the subcritical neutron multiplication factor is calculated. There is a count rate associated with the filling of the C-ring, and for every step thereafter until criticality is achieved. For each of these steps, the addition of fuel elements is modeled by replacing water-filled core locations with appropriate fuel element cells, and then k_{eff} is calculated.

3.4.4. Critical Control Rod Heights

The startup logs reflect that once the core has been filled out to the E-ring and the first seven fuel elements have been loaded into the F-ring, the

reactor has become critical. Upon reaching criticality, the control rods will be partially inserted into the core to prevent the core from being supercritical. The height of the control rods will reflect the steady-state position indicated on record in the startup log and the position of the control rods will be controlled in the same manner as discussed in §3.4.1. Where control rod positions are given, the fuel element maneuvers associated with the position will be reflected in the MCNP model and k_{eff} for the core will be calculated. It is expected that for these comparisons the calculation reflects the perfectly critical core.

3.4.5. Calculated Control Rod Worth

The MCNP model can be used to estimate the worth along the span of each control rod. To do this, all control rods begin in the ARI position. One rod is withdrawn in small increments and k_{eff} is measured at each step until the rod is fully withdrawn from the core. This process is repeated for each control rod, beginning every time from the ARI position. The reactivity insertion associated with k_{eff} for each partially withdrawn control rod position (k_1) can be calculated against the reference ARI case (k_0).

$$\rho\ (pcm) = 10^5 \times \frac{k_1 - k_0}{k_1 \times k_0}$$

3.4.6. Measured Control Rod Worth

Once the core has been loaded with fuel, testing is performed to determine the integral worth of each control rod (IRW). This is performed by starting with the rod of interest fully inserted with the other rods at (nearly) equal, partially withdrawn, critical rod heights and reactor power at 15W. The test rod is pulled a small increment and the stable reactor period is measured. This is followed by the SCRAM of one of the other partially withdrawn rods. Rod heights are adjusted to restore power to 15W without moving the position of the test rod. This procedure is continued with the rod of interest incrementally withdrawn by greater amounts and the same rod used for

SCRAM each time. An IRW curve can be created for each control as a result of this procedure.

Table 3-1 gives delayed neutron data for a TRIGA®.

Table 3-1. Delayed neutron data[15].

Delayed Neutron Group	1	2	3	4	5	6
Half Life (s)	56	23	6.2	2.3	0.61	0.23
β_i	0.000285	0.0015975	0.00141	0.0030525	0.00096	0.000195
β	0.0075					
λ_i (s^{-1})	0.01271	0.03173	0.1155	0.3108	1.397	3.872
β_i/λ_i	0.022423	0.050347	0.012208	0.009821	0.000687	.0000504
λ	0.0785038					

The reactor period recorded for each reactivity insertion can be converted to units of pcm with the delayed neutron fraction, β, and decay constant, λ, using the inhour equation.

$$\rho = \frac{\ell}{\ell + T} + \frac{T}{\ell + T} \times \sum_{i=1}^{6} \frac{\beta_i}{1 + \lambda_i T}$$

For each of the control rod pulls, the reactor period will be many seconds long, and the neutron lifetime will be very short. Using ℓ <<T and restricting the calculation to one delayed neutron group, some simplifications can be made to the inhour equation.

$$\frac{\ell}{\ell + T} \Rightarrow 0 \text{ and } \frac{T}{\ell + T} \Rightarrow 1 \text{ so } \rho \approx \sum_{i=1}^{6} \frac{\beta_i}{1 + \lambda_i T} \approx \frac{\beta}{1 + \lambda T}$$

Combining delayed neutron data,

$$\beta = \sum_{i=1}^{6} \beta_i \text{ and } \lambda = \beta \sum_{i=1}^{6} \frac{\lambda_i}{\beta_i}$$

4. Results / Discussion

The methodology discussed in the previous chapter was followed sequentially, beginning with updates and changes to the reactor model and followed by the chronological maneuvers and measurements associated with the initial post-conversion startup of the OSTR on LEU fuel. The results of calculations are discussed in the following sections.

4.1. Changes in Calculated Reactivity

Beginning with the original reactor model, changes were made individually and successively with a calculation for reactivity performed after each change. The magnitude of each difference in the model can be determined this way. The macroscopic effect of each consideration is presented within this section. Calculations described in §4.1 are all performed with the control rods 100% withdrawn from the core.

4.1.1. Initial Model

Prior to making any modifications to the model the reactivity of the original model was calculated. This is used as the basis from which the first changes are built. Table 4-1 gives the reactivity for the model and the standard deviation associated with the calculation.

Table 4-1. Calculated data for the initial core model.

Case	k_{eff}	σ
Initial Model	1.04870	0.00005

A bottom-up view of the reactor core and surrounding facilities is shown in Figure 4-1. This figure shows only two of the four beam ports incorporated into the model. Beam Port #3 is the tangential beam port extending from the northwest corner of the image and Beam Port #4 extends from the southwest corner.

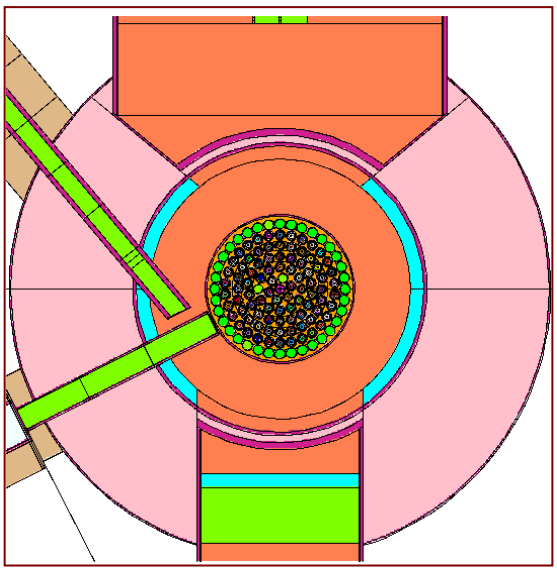

Figure 4-1. Bottom-up view of the initial core model.

4.1.2. Beam Ports

The first changes incorporated into the model are the addition of the two originally missing beam ports. Table 4-2 gives the calculated reactivity for the model with two, three, and four beam ports and the associated standard deviation. Additionally, the reactivity change for each case from the original is given. Both times, the addition of a beam port reduces the calculated reactivity.

Table 4-2. Calculated data for the addition of beam ports.

Beam Ports	k_{eff}	σ	Δρ (pcm)
3 and 4	1.04870	0.00005	0.0
1, 3, and 4	1.04764	0.00015	-96.5
1, 2, 3, and 4	1.04690	0.00016	-164.0

The same bottom-up view shown in Figure 4-1 is given in Figure 4-2 with Beam Port 1 added and in Figure 4-3 with Beam Port 2 also added. These figures correspond to the models with results given in Table 4-2**.**

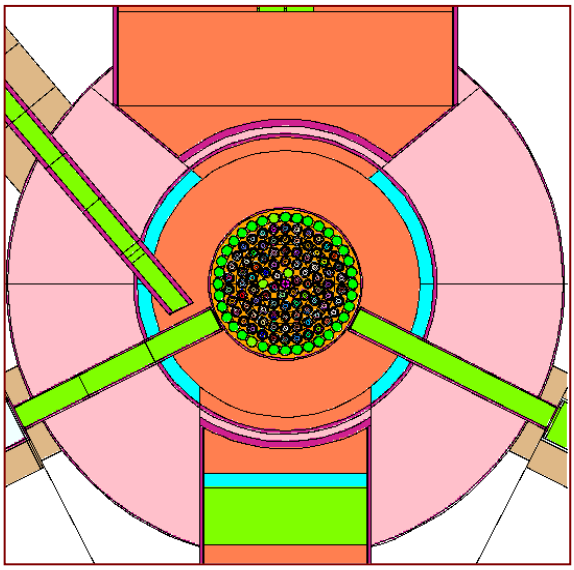

Figure 4-2. Bottom-up view of initial core model with beam port 1 added.

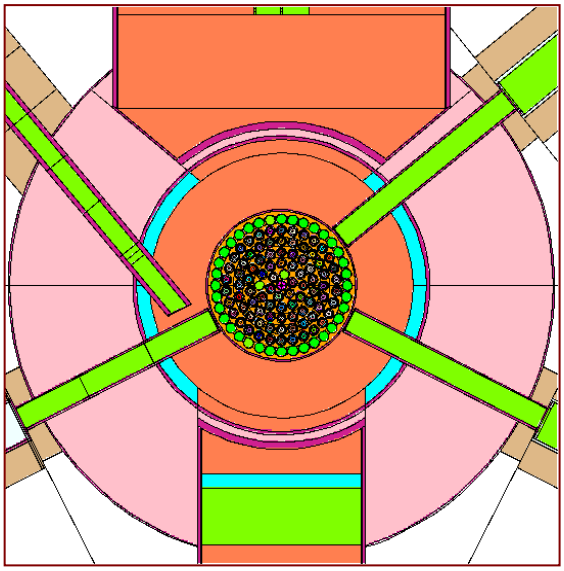

Figure 4-3. Bottom-up view of initial core model with all beam ports included.

Addition of beam port 1 reduced the calculated reactivity by 96.5 pcm ± 14 pcm (1σ). Addition of beam port 2 reduced the calculated reactivity by an additional 67.5 pcm ± 15 pcm (1σ). This reduction in reactivity can be attributed to greater neutron leakage from the core due to the close proximity of a neutron escape path at the beam port entrance. These reductions in k_{eff} are a

measurement by which the reactor model became more accurate with the addition of the beam ports.

4.1.3. Radial Reflector Water Saturation

Following the implementation of the correct beam port geometry, the level of water saturation in the radial graphite reflector was perturbed. The model from the previous section with all four beam ports implemented is used as the base case in this calculation beginning with 0% water in the reflector. The calculated reactivity and standard deviation is given in Table 4-3 for each 5% addition of water by volume. Also given in this table is the total change in reactivity associated with each case from the 0% case. The results of the calculation show that the addition of water to the beam port continues to add negative reactivity to the system.

Table 4-3. Calculated data for water saturation of the radial reflectors.

Volume % Water	k_{eff}	σ	Δρ (pcm)
0%	1.04690	0.00016	0.0
5%	1.04535	0.00016	-141.6
10%	1.04469	0.00016	-202.1
15%	1.04385	0.00015	-279.1
20%	1.04311	0.00016	-347.1
25%	1.04254	0.00016	-399.5
30%	1.04195	0.00017	-453.8

The data given in Table 4-3 is represented graphically in Figure 4-4. Error bars representing one standard deviation appear for each data point. The standard deviation is much smaller than the trending decrease in calculated reactivity and a greater amount of water in the reflector lends itself to a potentially significant decrease in the results of the calculation.

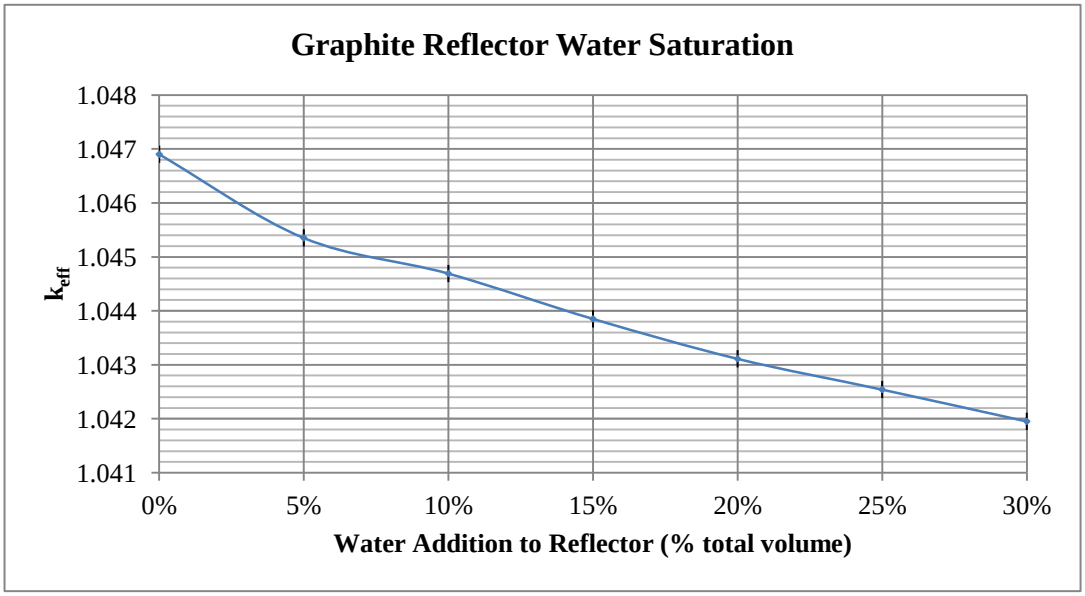

Figure 4-4. Reactivity curve for water saturation of the graphite reflector.

Following investigation of the effects of water saturation of the graphite reflector, the model incorporated an additional composition of water equivalent to 30% of the volume of the reflector. The volume of the reflector was not increased, so the result was a much denser material. The change from 0% to 30% water saturation by volume is characterized by a decrease in reactivity of 454 pcm ± 16 pcm (1σ).

A possible explanation for this large decrease in reactivity is the over moderation of neutrons that occurs in the reflector. Neutrons that advance to the reflector undergo far more scattering collisions because the atomic density has increased so much. Neutrons lose enough energy through scattering that they are no longer energetic enough to travel back into the core, and they become lost from the system.

From the preceding cases, the configuration with 30% water saturation was accepted as the basis for the continued downstream calculations. The justification for this decision is due to the fact that the aluminum clad surrounding the reflector has failed. It is not difficult to justify that 30% of the volume of the reflector could be made up by water just by compensating for the

deficiency in achievable theoretical density. It is possible that far more than 30% of the volume could be made up by water when accounting for water molecules occupying vacant sites within the lattice, as well. Until the actual composition of the fuel is known with certainty, this assumption is reasonable.

4.1.4. As-Built Fuel

Every calculation to this point incorporated a generic definition for the fuel composition with every fuel element comprised of identical weight fractions of each isotope in the fuel, and without the inclusion of many impurities. The generic fuel was switched for the as-built compositions of every constituent isotope in the fuel as well as all of the measured impurities. The results of the calculation for both approaches to modeling the fuel are given in Table 4-4.

Table 4-4. Calculated data for incorporation of as-built fuel.

Fuel	k_{eff}	σ	Δρ (pcm)
Generic	1.04195	0.00017	0.0
As-Built	1.05175	0.00016	894.3

Incorporation of the as-built fuel rather than uniformly assigned material compositions had a positive effect on reactivity. This change added 894 pcm of reactivity, ± 15 pcm (1σ). The as-built fuel includes all measurable impurities as well.

A more accurate representation of the fuel introduces a significant amount of reactivity to the reactor model. The most significant difference between the old fuel model and the as-built fuel is the uranium content. The atom density of ^{235}U in the old model was 1.0829×10^{-3} atoms per barn-cm. The as-built fuel has an average ^{235}U atom density of 1.0917×10^{-3} atoms per barn-cm. The represents a 0.812% increase in the atom density of ^{235}U in the change from the old fuel model to the new. Although this is a fractionally small amount, this great of an increase in the amount of fissile material in the core will inevitably have a large impact on the reactivity of the core. An additional

change with the as-built fuel is the erbium loading. Less erbium is loaded into the center of the core, allowing for a more efficient fuel configuration. In general, this results in higher k_{eff} results.

Differences between other elements and isotopes exist between the two models, however, the overall effect tends to be cancelling, and no other elements with appreciable difference have such influence over reactivity.

Figure 4-5 is a bottom-up view of each fuel element loaded into the core. Although many calculations and core configurations do not require all fuel elements to be loaded into the core, the comparison between the generic fuel definition and the as-built, exact fuel composition considers every fuel element loaded for both calculations.

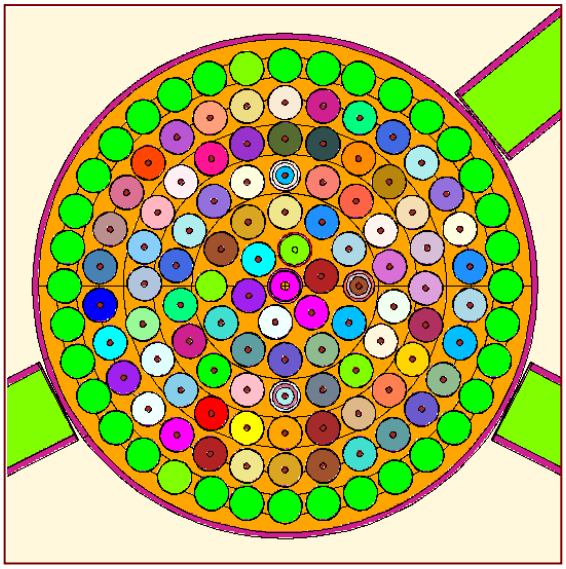

Figure 4-5. Bottom-up view of reactor core with as-built fuel compositions.

4.1.5. Hafnium Impurities

Impurities in the fuel are measured for each fuel meat so the weight percent of each impurity is known and incorporated into the total composition of the fuel material. The amount of hafnium found in the fuel was only measured for two fuel batches and does not give a thorough representation of how much hafnium may be present throughout the core. Because hafnium has

very strong thermal neutron absorption properties, the potential exists for a great deal of sensitivity to this parameter. Perturbations from the assumed average concentration of 7.5 μg per g of fuel were used to characterize the sensitivity introduced to the system reactivity by hafnium. The weight percent was calculated from 5.0 to 10.0 μg hafnium per g of fuel in increments of 0.5 μg increments and the results of each calculation is given in Table 4-5.

Table 4-5. Calculated data for perturbations to hafnium concentrations.

Hf Weight %	k_{eff}	σ	Δρ (pcm)
5.0%	1.05182	0.00008	0.0
5.5%	1.05169	0.00008	-11.8
6.0%	1.05173	0.00008	-8.1
6.5%	1.05193	0.00008	9.9
7.0%	1.05186	0.00008	3.6
7.5%	1.05169	0.00008	-11.8
8.0%	1.05172	0.00008	-9.0
8.5%	1.05158	0.00008	-21.7
9.0%	1.05168	0.00008	-12.7
9.5%	1.05162	0.00008	-18.1
10.0%	1.05174	0.00008	-7.2

The change in reactivity was calculated for hafnium weight percent from 5.0 to 10.0 μg per g. Because the hafnium is changed in very small amounts, correspondingly small changes in reactivity may also be expected. For this reason, the fidelity of the calculation was taken into consideration and more total neutrons were used in the calculation, resulting in a smaller standard deviation than prior calculations. However, the standard deviation still remained on the order of the same size as the reactivity change from case to case. Figure 4-6 shows the magnitude of the standard deviation with the reactivity results of the perturbation. Over the range of weight percents considered, the results change only very small amounts. Although it is expected that the reactivity decreases with greater concentrations of a strongly absorbing material, the trend is not definitively seen when taking into account the size of the standard deviation.

Hafnium concentrations were considered at concentrations well outside the bounds of the tolerance of the measurement to determine if any sensitivity exists in the hafnium concentration in the fuel, or its associated measurement uncertainties. The difference in reactivity from the smallest (8.5 $x10^{-6}$ wt%) to the largest (6.5 $x10^{-6}$ wt%) resulting k_{eff} was 32 pcm ± 7 pcm (1σ). This amount of reactivity difference has a negligible impact on the calculated reactivity of the core. In addition to being a negligible impact, there is no obvious trend in a decrease in reactivity associated with an increase in hafnium concentration, as would be expected. For these reasons, the $7.5x10^{-6}$ wt% hafnium concentration is deemed acceptable, and is applied to each fuel element.

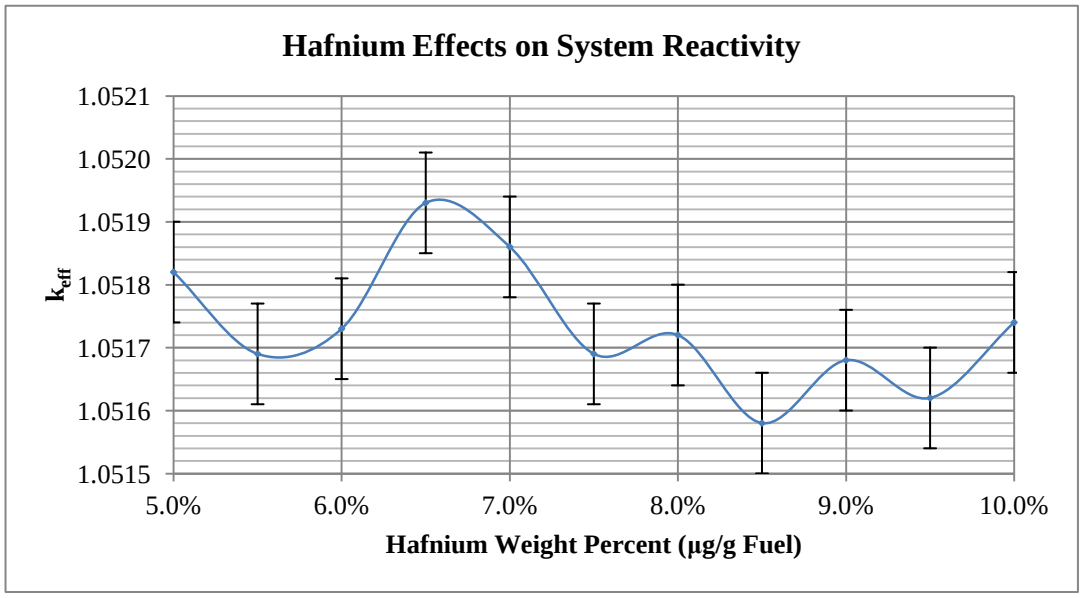

Figure 4-6. Reactivity curve for changes in hafnium concentrations.

The total amount of hafnium included in the modeled fuel remains the average of 7.5 µg hafnium per g of fuel, and small changes to this parameter do not appear to have any significant affect on reactivity.

4.1.6. Nuclear Data Library

With the implementation of every planned model change, a known critical configuration is used to explore the reactivity effects associated with data libraries for zirconium. Every attempt to reflect the actual geometry and

materials of the OSTR has been made and the critical configuration reflects a core with a majority of the fuel elements loaded and has the control rods at levels partially inserted. With the expectation that the results of a criticality calculation should reflect that the core is exactly critical, changes in the zirconium data used have the potential to show their impact on the bias between calculated and measured reactivity results.

Various cases are considered which utilize different combinations of zirconium in the model on both material and material data cards and the version of ENDF cross section data used for the calculation. The first cross section data calculation had all material cards updated to ENDF/B-VII data, but all mt cards still use ENDF/B-V data. The considerations to the second cross section calculation changes the mt cards for graphite and light water to ENDF/B-VII cross section data. This change is maintained for the remainder of the cross section data calculations. There is no presupposed error in data for these materials, and using ENDF/B-VII data is reasonable. This change results in a 26.8 pcm reactivity insertion. The third cross section calculation builds on the previous change, and additionally changes the mt cards for zirconium in hydrogen (zr/h) and hydrogen in zirconium (h/zr) from ENDF/B-V to ENDF/B-VI data, and this resulted in a 154.6 pcm reactivity insertion. The fourth cross section calculation is similar to the third, except instead of using ENDF/B-VI data for zr/h and h/zr, ENDF/B-VII is used. The addition in reactivity is slightly less, being only 137.7 pcm this time. The fifth cross section calculation models zr/h and h/zr with ENDF/B-VI like in the third calculation, except this time elemental/isotopic zirconium is also modeled with ENDF/B-VI. The result is a 69.5 pcm negative reactivity insertion. The sixth calculation is similar to the fifth, except hydrogen is also modeled with the ENDF/B-VI library. The result is only a 21.8 pcm negative reactivity insertion. In the seventh calculation, every material is modeled with the ENDF/B-VII cross section library except for elemental/isotopic zirconium. The result is a 36.7 pcm negative reactivity

insertion compared to the first case. The eighth and final case is the same as the seventh, except both zirconium and hydrogen are modeled with the ENDF/B-VI library and result in a 10.9 pcm reactivity insertion.

The results of the calculated reactivity are given in Table 4-6, as well as the relative change in reactivity for each case from the first case.

Table 4-6. Reactivity effects from various combinations of nuclear libraries.

Library Set	k_{eff}	σ	Δρ (pcm)	Description
1	1.00385	0.00016	0.0	All mt cards ENDF5, all fuel materials ENDF7
2	1.00412	0.00015	26.8	All mt cards for grph and lwtr changes to ENDF7, all fuel materials ENDF7
3	1.00541	0.00016	154.6	grph and ltwr mt ENDF7, change h/zr and zr/h to ENDF6, all fuel materials ENDF7
4	1.00524	0.00016	137.7	grph and ltwr mt ENDF7, change h/zr and zr/h to ENDF7, all fuel materials ENDF7
5	1.00315	0.00016	-69.5	grph and ltwr mt ENDF7, h/zr and zr/h to ENDF6, ENDF6 zirconium, all other fuel materials ENDF7
6	1.00363	0.00017	-21.8	grph and ltwr mt ENDF7, h/zr and zr/h to ENDF6, ENDF6 zirconium and hydrogen, all other fuel materials ENDF7
7	1.00348	0.00016	-36.7	grph and ltwr mt ENDF7, h/zr and zr/h to ENDF7, ENDF6 zirconium, all other fuel materials ENDF7
8	1.00396	0.00017	10.9	grph and ltwr mt ENDF7, h/zr and zr/h to ENDF7, ENDF6 zirconium and hydrogen, all other fuel materials ENDF7

The expected result is that zirconium is most accurately represented by ENDF/B-VI, and this data should be used in the model until more accurate data is available. This would be consistent with the findings of the NRAD LEU benchmarking results. The results of this calculation show that when all material data is defined by ENDF/B-VII with the exception of zirconium defined by ENDF/B-VI, the greatest decrease in reactivity is seen. For the

critical case considered here, this is the desired outcome because the model over-predicts the reactivity of the reactor. Modifying the cross section data used helps to correct the calculated value in the direction of the measured value.

Although ENDF/B-VII is the most current neutron cross section data library available, other version of ENDF libraries were considered for modeling zirconium. The outcome was that all elements and isotopes would be modeled using the current version of ENDF/B-VII. However, zirconium, zirconium in hydrogen, and hydrogen in zirconium were to be represented by ENDF/B-VI. The difference between modeling all materials in ENDF/B-VII and modeling zirconium in ENDF/B-VI is a decrease in reactivity of 69.5 pcm ± 16 pcm (1σ).

4.2. Reactor Critical Calculations

Following the implementation of each of the previously explored modifications the model is frozen in this final form. This version of the model is then used to mimic the initial loading of the core and measurements taken during the approach to critical. The addition of new fuel began on Wednesday, October 1st of 2008 (Day 1), and modeled comparisons are made to operations and measurements that occur through Wednesday October 15th of 2008 (Day 15).

4.2.1. Approach to Critical

Beginning from an empty core, fuel was loaded gradually until criticality was achieved. Each fuel element ever resides only in a single assigned location. A label for each fuel element location is given in Figure 4-7.

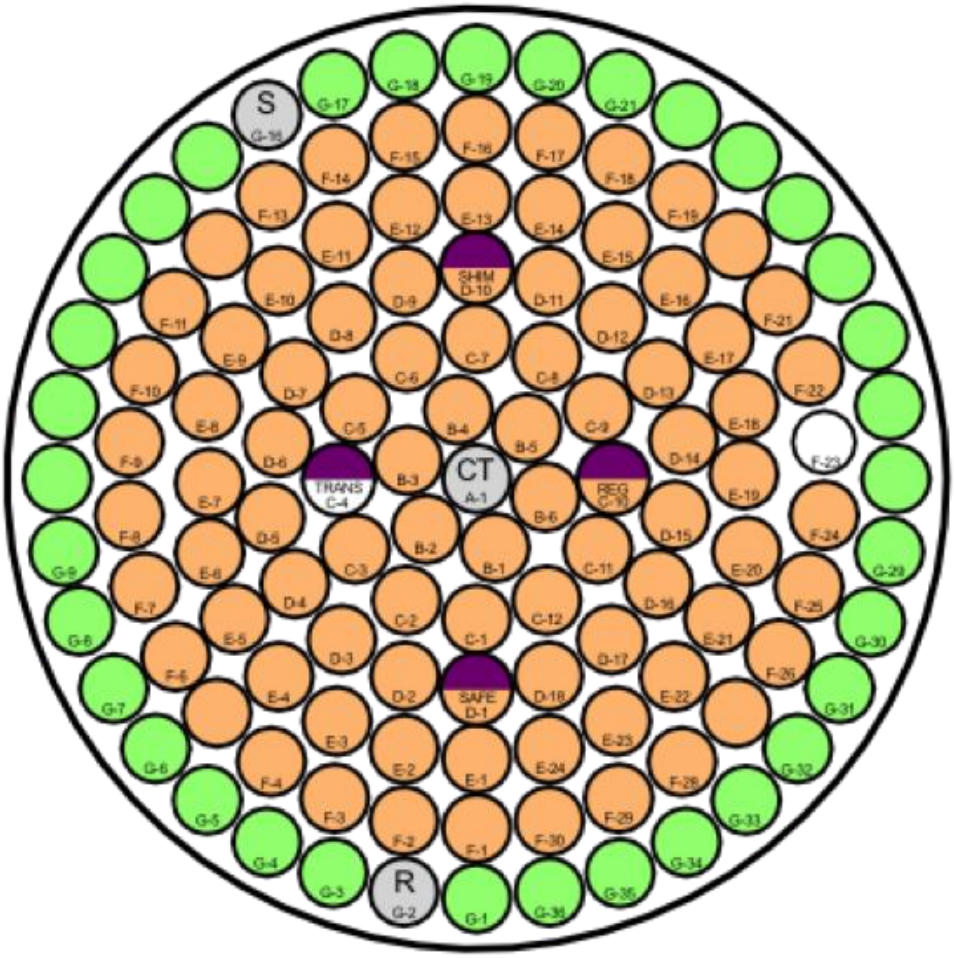

Figure 4-7. Fuel element location labeling.

Before any fuel was loaded into the core, the four control rods were positioned in the full withdrawn position on Day 1. The regulating, safety, and shim rods are fuel-followed, so with the control rods in the fully withdrawn position, there were effectively three fuel elements loaded into the core. No count rate was measured at this point, but an MCNP calculation estimates k_{eff} for the system to be 0.26430 with a standard deviation of 0.00008. In the afternoon of Day 2 the B-4 fuel element was loaded and in the afternoon of Day 3 the B-2 fuel element was loaded.

In the morning of Day 6, the remaining four fuel elements in the B-ring were loaded. No count rate was measured at this point, but an MCNP

calculation estimates k_{eff} for the system with nine fuel elements loaded to be 0.54745 with a standard deviation of 0.00014. Still in the morning of Day 6, the ten C-ring fuel elements were loaded. Including the two control rods in the C-ring, this ring was now also filled, in addition to the B-ring. Around noon of Day 6, measurements indicated a count rate of 36.8 cps, and an MCNP calculation estimated k_{eff} for the system to be 0.75060 with a standard deviation of 0.00016.

In the afternoon of Day 6, eight fuel elements were loaded into the D-ring (D-2 through D-9) and two fuel elements were loaded into the E-ring (E-6 and E-7). The fuel element in position D-8 was then removed, but replaced in the morning of Day 7. At that time, measurements indicated a count rate of 37.3 cps, and an MCNP calculation estimates k_{eff} for the system to be 0.84559 with a standard deviation of 0.00016.

In the morning of Day 7, eight additional fuel elements were loaded into the D-ring (D-11 through D-18) and two additional elements were loaded into the E-ring (E-18 and E-19). Following the loading of these fuel elements, the D-ring was completely filled. Measurements indicated a count rate of 52.9 cps, and an MCNP calculation estimated k_{eff} for the system to be 0.90348 with a standard deviation of 0.00016.

Later in the morning of Day 7, fuel elements E-1 through E-4 were loaded with measurements indicating a count rate of 55.3 cps, and an MCNP calculation estimated k_{eff} for the system to be 0.92236 with a standard deviation of 0.00016. Fuel elements were then loaded into positions E-5 and E-8 through E-10, and measurements indicated a count rate of 55.9 cps, and an MCNP calculation estimated k_{eff} for the system to be 0.93860 with a standard deviation of 0.00017. The last maneuver performed in the morning of Day 7 was fuel elements added to positions E-11 through E-14. Measurements indicated a count rate of 65.0 cps, and an MCNP calculation estimated k_{eff} for the system to be 0.95497 with a standard deviation of 0.00016.

In the afternoon of Day 7, fuel elements were added to locations E-15 through E-17 and E-20. Measurements indicated a count rate of 101.0 cps, and an MCNP calculation estimated k_{eff} for the system to be 0.96934 with a standard deviation of 0.00016. This was followed by fuel elements added to locations E-21 through E-24, resulting in the E-ring being filled completely. Measurements indicated a count rate of 156.7 cps, and an MCNP calculation estimated k_{eff} for the system to be 0.98244 with a standard deviation of 0.00016. With the addition of fuel elements in positions F-1 through F-4, measurements indicated a count rate of 298.3 cps, and an MCNP calculation estimated k_{eff} for the system to be 0.99330 with a standard deviation of 0.00016.

Count rates indicated that the reactor configuration was nearing critical, and fuel elements were loaded individually at this point. Following the filling of the F-5 location, measurements indicated a count rate of 424.8 cps, and an MCNP calculation estimated k_{eff} for the system to be 0.99549 with a standard deviation of 0.00015. After loading the F-6 location, measurements indicated a count rate of 796.4 cps, and an MCNP calculation estimated k_{eff} for the system to be 0.99788 with a standard deviation of 0.00016. After loading fuel into the F-7 location, measurements indicated that the reactor achieved criticality. An MCNP calculation for this critical configuration estimated k_{eff} for the system to be 1.00085 with a standard deviation of 0.00016.

In agreement with startup measurements, MCNP calculations indicate that the transition from 65 to 66 fuel elements in the core corresponds to the reactor transitioning from a subcritical to a critical configuration.

These fuel maneuvers, measurements, and comparative calculations are summarized in Table 4-7.

Table 4-7. Core loading and calculations for the approach to critical.

Fuel Elements	k_{eff}	σ	CR (cpm)	Description
3	0.26430	0.00008	-	All control rods loaded, ARO.
9	0.54745	0.00014	-	Six elements added to the B-ring; B-ring is full.
19	0.75060	0.00016	36.8	Ten elements added to the C-ring; C-ring is full.
29	0.84559	0.00016	37.3	Eight elements added to the D-ring and two to the E-ring.
39	0.90348	0.00016	52.9	Eight elements added to the D-ring and two to the E-ring; D-ring is full.
43	0.92236	0.00016	55.3	Four elements added to the E-ring.
47	0.93860	0.00017	55.9	Four elements added to the E-ring.
51	0.95497	0.00016	65.0	Four elements added to the E-ring.
55	0.96934	0.00016	101.0	Four elements added to the E-ring.
59	0.98244	0.00016	156.7	Four elements added to the E-ring; E-ring is full.
63	0.99330	0.00016	298.3	Four elements added to the F-ring.
64	0.99549	0.00015	424.8	One element added to the F-ring.
65	0.99788	0.00016	796.4	One element added to the F-ring.
66	1.00085	0.00016	-	One element added to the F-ring; reactor is supercritical.

The transition from a subcritical configuration with 65 fuel elements to a critical configuration with 66 fuel elements is shown in Figure 4-8 and Figure 4-9. Most of the outer ring of fuel elements is not loaded with fuel, and these water-filled locations are all indicated by the same color. The difference between these two figures is the F-ring containing either six or seven fuel elements. The fuel element added that causes the core to have a critical

configuration is F-7 in the northwest corner of the F-ring, as it shown in the following figures.

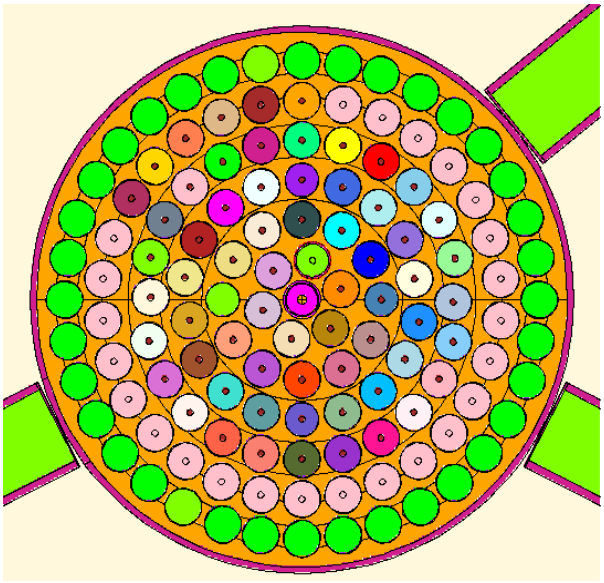

Figure 4-8. Bottom-up view of core immediately prior to criticality.

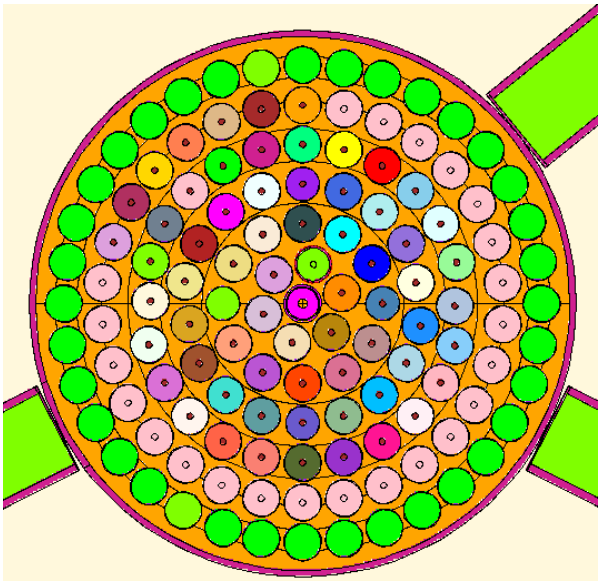

Figure 4-9. Bottom-up view of core immediately following criticality.

4.2.2. Critical Configuration

Once enough fuel has been added to the core so that criticality is achieved, all further maneuvers and operations require that the control rods be partially inserted in order to compensate for the excess reactivity in the core. The remainder of the fuel movements and operations during startup testing have specific steady-state critical rod heights associated with them. The remaining fuel elements were added in turn to the core and measurements continued to be taken. Each new core configuration is modeled with its measured critical rod height. The reactivity of the system should be such that the control rods are inserted the appropriate amount to perfectly offset the core excess reactivity (the core should be perfectly critical with k_{eff}=1.0). Each of these configurations with critical rod heights is modeled in MCNP and the reactivity is measured to compare the accuracy of the modeled system against the actual startup data.

As discussed previously, a critical configuration was achieved in the afternoon of Day 7 of the LEU conversion and startup testing. Following the achievement of criticality, position F-8 was filled, and the first critical rod heights were recorded. The transient rod was 60.0% withdrawn, the safety rod was 100.0% withdrawn, the shim rod was 100.0% withdrawn, and the regulating rod was 74.7% withdrawn. These critical rod heights will be denoted as [#1: Tr 60.0; Sa 100.0; Sh 100.0; Reg 74.7]. A model of this configuration resulted in an estimated calculated k_{eff} of 1.00080 with a standard deviation of 0.00016.

Following a number of reactor maneuvers and measurements at or below 15 W on Day 7, there were no reactor operations on Day 8.

In the afternoon of Day 9 operations began again and the second critical rod heights were recorded. [#2: Tr 100.0; Sa 86.0; Sh 86.0; Reg 82.1] The k_{eff} for this configuration was 1.00045 with a standard deviation of 0.00017. Following this, reactor power was increased from 15 W to 1000 W and integral rod worth measurements were performed. Following these measurements the

reactor was shut down and fuel elements were loaded into the F-9 through F-12 positions. New critical rod heights were recorded. [#3: Tr 72.6; Sa 72.7; Sh 72.6; Reg 72.7] The k_{eff} for this configuration was 1.00151 with a standard deviation of 0.00017. Following this, the reactor power was again raised from 15 W to 1000 W and integral rod worth measurements were taken again before shutting down the reactor at the end of the day.

On the morning of Day 10, fuel elements were loaded into positions F-13 through F-16. At 15 W [#4: Tr 63.3; Sa 63.3; Sh 63.3; Reg 63.2], the k_{eff} for this configuration was 1.00219 with a standard deviation of 0.00016. Integral rod worth measurements were again taken that morning with the reactor power raised from 15 W to 1000 W. Following these measurements, the reactor was shut down. Later in the morning of Day 10, fuel elements were loaded into positions F-17 through F-20.

In the afternoon of Day 10, another set of critical rod heights at 15 W was recorded. [#5: Tr 56.2; Sa 56.2; Sh 56.2; Reg 56.2] The k_{eff} for this configuration was 1.00269 with a standard deviation of 0.00016. Power was raised from 15 W to 1000 W and integral rod worth measurements were taken. Following these measurements, the reactor was shut down and fuel elements were added to the F-26, F-27, F-29, and F-30 locations. Reactor power was again brought to 15 W and critical rod heights were recorded. [#6: Tr 50.1; Sa 49.9; Sh 49.9; Reg 50.1] The k_{eff} for this configuration was 1.00262 with a standard deviation of 0.00017. Again in the afternoon of Day 10, reactor power was increased to 1000 W, integral rod worth measurements were taken, and the reactor was shut down. The final fuel maneuver on Day 10 was the loading of fuel into the F-21 through F-24 locations.

At the end of Day 10, the core configuration reflects that of a core fully loaded with fuel with the exception of the F-25 and F-28 locations.

On the morning of Day 13, steady-state, 15 W critical rod heights were recorded [#7: Tr 42.7; Sa 42.7; Sh 42.7; Reg 42.5]. The k_{eff} for this

configuration was 1.00256 with a standard deviation of 0.00017. The reactor power was increased from 15 W to 1000 W, and critical rod heights were found [#8: Tr 100.0; Sa 31.2; Sh 31.2; Reg 31.1]. The k_{eff} for this configuration was 1.00551 with a standard deviation of 0.00016. Integral rod worth calculations were again performed, then the reactor was shut down.

While shut down, a fuel element was loaded into the F-25 location. With every fuel element location filled with the exception of F-28, critical rod heights [#9: Tr 41.7; Sa 41.7; Sh 41.7; Reg 41.8] were found giving a calculated k_{eff} of 1.00275 with a standard deviation of 0.00015. Reactor power was raised to 1000 W, integral rod worth measurements were taken, and the reactor was shut down.

On the afternoon of Day 13, rod calibration measurements began. Prior to these measurements, a critical configuration was found [#10: Tr 0.0; Sa 51.0; Sh 51.0; Reg 50.1] which gave a calculated k_{eff} of 1.00315 with a standard deviation of 0.00016. Using the period method, incremental rod worths were calculated for the transient, safety, and shim control rods for the remainder of the afternoon.

On the morning of Day 14, incremental rod worths were calculated for the regulating control rod. Each of the incremental rod worth calculations was performed at 15 W and each has numerous critical rod height configurations associated with it. The incremental rod worths will be discussed in upcoming sections.

Following the last of the rod calibration measurements performed on the morning of Day 14, the fuel element was removed from location F-16 and a critical configuration was found [#11: Tr 38.0; Sa 38.0; Sh 38.0; Reg 53.3] which gave a calculated k_{eff} of 1.00269 with a standard deviation of 0.00016. Later in the morning, the fuel element was loaded back into the F-16 location and another fuel element was removed from the F-12 location. Critical rod heights [#12: Tr 38.0; Sa 38.0; Sh 38.0; Reg 53.2] gave a calculated k_{eff} of

1.00247 with a standard deviation of 0.00016. The fuel element in the F-12 location was replaced, and another fuel element was removed from the F-9 location, and critical rod heights [#13: Tr 38.0; Sa 38.0; Sh 38.0; Reg 53.9] gave a calculated k_{eff} of 1.00196 with a standard deviation of 0.00015. The reactor was shut down, no additional fuel maneuvers were performed, then it was turned back on again. Critical rod heights [#14: Tr 38.0; Sa 38.0; Sh 38.0; Reg 49.9] gave a calculated k_{eff} of 1.00079 with a standard deviation of 0.00016.

All of the fuel maneuvers that occurred with a critical core configuration and the associated calculated parameters are summarized in Table 4-8.

Table 4-8. Calculated data for critical core configurations.

Config.	# FE	k_{eff}	σ	Power (W)	Description
1	67	1.00080	0.00016	15	One fuel element added to F-ring.
2	67	1.00045	0.00017	15	No fuel elements added.
3	71	1.00151	0.00017	15	Four fuel elements added to F-ring.
4	75	1.00219	0.00016	15	Four fuel elements added to F-ring.
5	79	1.00269	0.00016	15	Four fuel elements added to F-ring.
6	83	1.00262	0.00017	15	Four fuel elements added to F-ring.
7	87	1.00256	0.00017	15	Four fuel elements added to F-ring.
8	87	1.00551	0.00016	1000	No fuel elements added.
9	88	1.00275	0.00015	15	One fuel element added to F-ring.
10	88	1.00315	0.00016	15	No fuel elements added.
11	87	1.00269	0.00016	15	One fuel element removed from F-ring.
12	87	1.00247	0.00016	15	One fuel element added and one removed from F-ring.
13	87	1.00196	0.00015	15	One fuel element added and one removed from F-ring.
14	87	1.00079	0.00016	15	No fuel elements added.

The result of the calculations for the first 14 low-power critical configurations is shown in Figure 4-10.

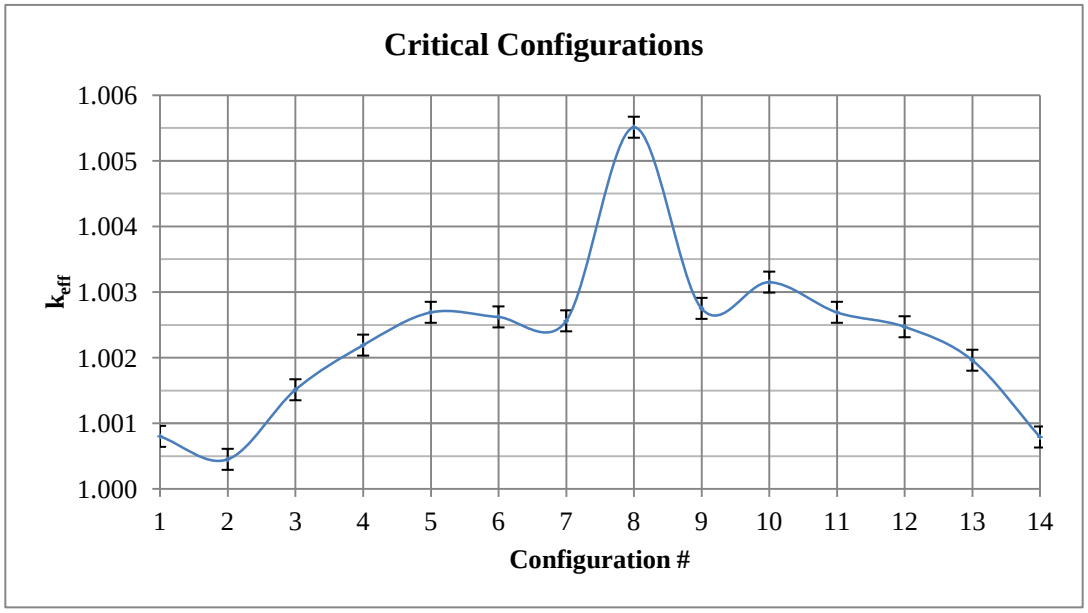

Figure 4-10. Reactivity curve for all critical configurations.

With the exclusion of critical configuration #8, the data shows a consistent trend of over-estimating the value of k_{eff}. It can be argued that this data point be excluded because the measurements occur when the reactor is at 1000 W, while all other measurements are for steady-state operation at 15 W.

The reason to exclude this data point is because an increase in core power results in negative reactivity insertion. To compensate, the control rods do not have to be inserted so far into the core. For critical configuration #8, the control rods have been slightly removed, however no other information is provided in the model to accurately portray the higher fuel and local coolant temperature. The model is still performing calculations at cooler temperatures, however the rods are removed slightly because of the higher temperature conditions. The result is that the calculated k_{eff} will be higher than it is in reality.

The ten included data points can be seen in Figure 4-11.

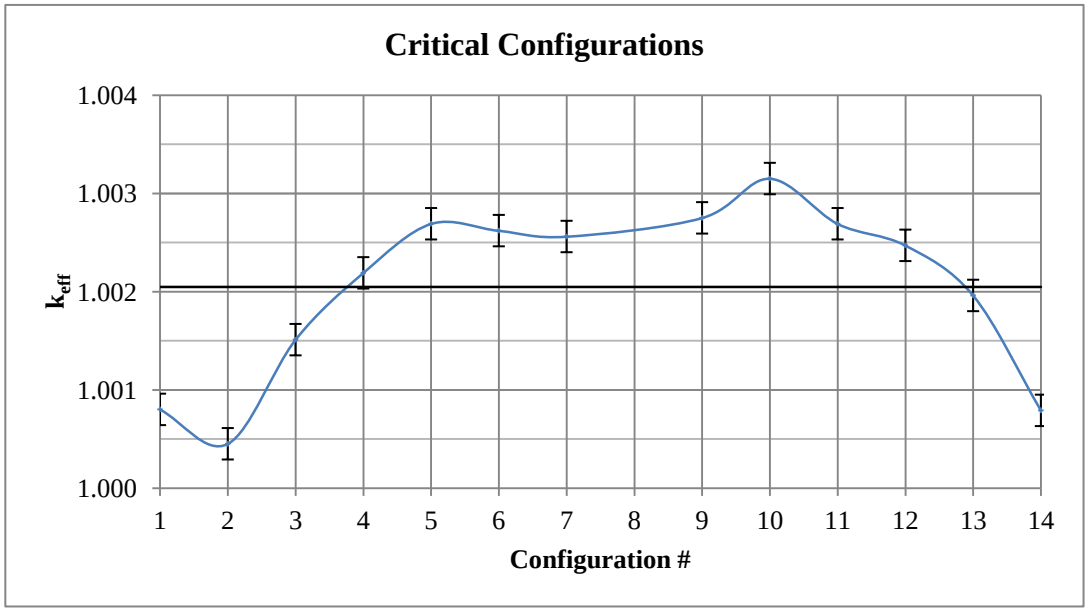

Figure 4-11. Reactivity curve for critical calculations occurring at low power.

Figure 4-11 has an additional curve at k_{eff}=1.00205. This line represents the arithmetic mean of the critical configurations. If we assume that β for this clean core fueled with ^{235}U is 0.0075, this k_{eff} corresponds to a \$0.273 bias.

4.2.3. Control Rod Worth

Besides calculating a global k_{eff} based on critical core configurations and control rod heights, comparing calculated and measured data for the integral and differential worths of the control rods provides additional benchmarking information. Incremental worths were measured for each control rod, which provide insight into the axial worth of each rod using the period method. The various control rod configurations required to perform these measurements can be modeled and the reactivity compared. Then the incremental worth predicted by the MCNP model of the core can be calculated. Each of these sets of control rod information can be used to give a developed characterization of the control rods and help to diversify the benchmarking comparisons.

The core margin (all rods in) and excess (all rods out) is given in Table 4-9. These configurations represent the least and most reactive control rod configurations for the OSTR with a cold clean core.

Table 4-9. Calculated data for bounding control rod positions.

	k_{eff}	σ	ρ (pcm)
All Rods In	0.96905	0.00016	-3193.8
All Rods Out	1.05029	0.00015	4788.2

4.2.3.1. Modeled Control Rod Worth

When measuring the control rod worth as discussed in the previous section, a critical control rod configuration at steady state operation is required prior to each incremental pull of a control rod. This results in a number more of critical configurations that can be used as further comparison of the measured and modeled core.

Table 4-10. Calculated data from critical control rod heights.

		% Withdrawn					
Conf.	**Rod Measured**	**Transient**	**Safety**	**Shim**	**Regulating**	**k_{eff}**	**σ**
15	Regulating	0.0	51.0	51.0	50.1	1.00406	0.00033
16	Regulating	22.4	47.0	47.0	47.3	1.00300	0.00036
17	Regulating	33.8	43.0	43.0	45.5	1.00237	0.00031
18	Regulating	44.1	40.0	40.0	42.1	1.00362	0.00035
19	Regulating	55.0	37.0	37.0	38.3	1.00349	0.00033
20	Regulating	67.2	34.0	34.0	34.8	1.00454	0.00029
21	Regulating	80.9	31.0	31.0	32.3	1.00490	0.00031
22	Safety	48.0	0.0	48.0	52.5	1.00392	0.00031
23	Safety	45.0	22.8	45.0	49.1	1.00410	0.00034
24	Safety	43.0	34.8	43.0	44.3	1.00326	0.00032
25	Safety	41.0	45.4	41.0	39.7	1.00281	0.00035
26	Safety	38.0	56.2	38.0	36.7	1.00279	0.00035
27	Safety	34.0	70.0	34.0	34.2	1.00392	0.00033
28	Shim	49.9	49.9	0.0	50.1	1.00262	0.00035
29	Shim	46.7	46.7	23.0	46.7	1.00357	0.00035
30	Shim	43.6	43.6	35.0	43.6	1.00265	0.00030
31	Shim	40.4	40.4	45.6	40.6	1.00294	0.00029
32	Shim	37.3	37.2	56.4	37.3	1.00343	0.00033
33	Shim	34.1	34.1	68.7	34.2	1.00412	0.00032
34	Transient	54.0	54.0	54.6	0.0	1.00485	0.00035
35	Transient	50.4	50.4	50.4	19.2	1.00381	0.00028
36	Transient	46.6	46.6	46.6	29.8	1.00341	0.00033
37	Transient	42.8	42.8	42.8	38.8	1.00349	0.00030
38	Transient	39.0	39.1	38.9	47.3	1.00292	0.00032
39	Transient	35.1	35.1	35.2	56.3	1.00289	0.00031
40	Transient	31.4	31.4	31.4	66.0	1.00247	0.00033
41	Transient	28.8	28.8	28.8	77.8	1.00520	0.00030
42	NA	38.0	38.0	38.0	49.9	1.00294	0.00032

The result of the calculations of the first 41 low-power critical configurations described in Table 4-8 and Table 4-10 is shown in Figure 4-12.

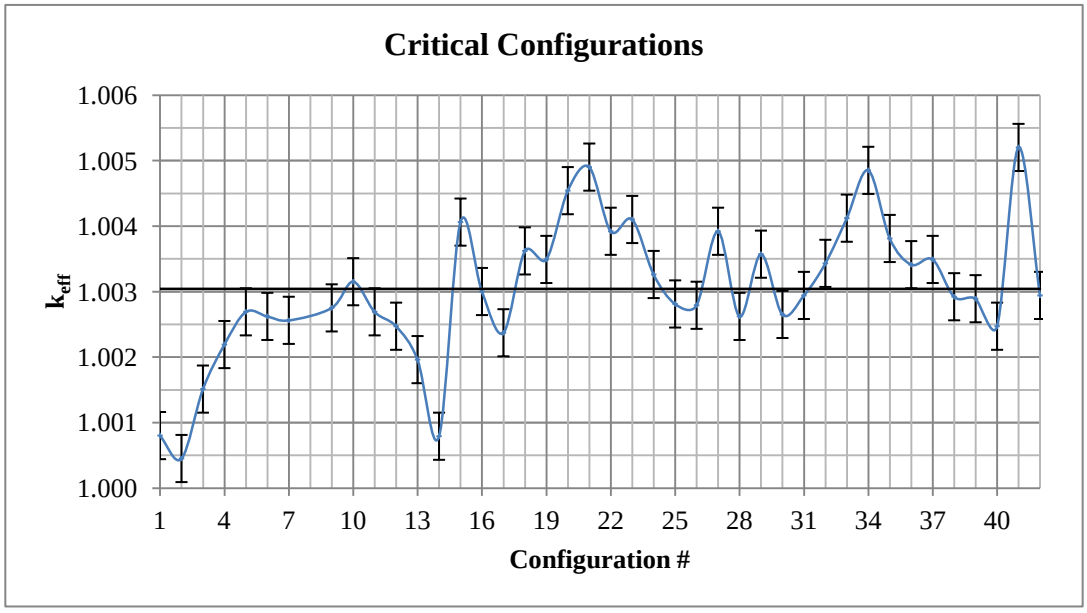

Figure 4-12. Calculated reactivity for all critical configurations.

Following the incorporation of the aforementioned changes, 42 critical configurations were modeled. Every configuration resulted in consistent results and a reactivity calculation greater than unity. The average calculated reactivity was a k_{eff} of 1.00304. The standard deviation of these calculations varied, but the greatest absolute error associated with the critical configuration comparisons was 0.00036 (1σ). Average excess reactivity is then 303 pcm, equivalent to \$0.405. Prior to this, the bias of the LEU core was carried forward and was primarily assumed to be the same as that of the HEU core, \$0.64 ± \$0.14.

4.2.3.2. Calculated Control Rod Worth

Each method of determining control rod worth will result in slightly different results because of the configuration of each of the control rods and the reactivity distribution in the core. The calculated worth of the control rods can be determined using the MCNP model. Although the combination of control rod heights used for these calculations and the associated k_{eff} values calculated are not reproducible in the core, they align with the reactor

model calculations similarly to the way control rod worth measurements of the actual rods align with the measured data.

For each calculation, all rods begin in the fully inserted position and reactivity is calculated. Each rod is individually withdrawn in small steps and k_{eff} is recalculated for each position. The total worth of the rod up to the point it is withdrawn can be directly calculated from the difference between the ARI position and the partially withdrawn position.

In Table 4-11 k_{eff} of the core with the regulating rod withdrawn incrementally is given with the standard deviation. Additionally, the worth of the rod is given from the incrementally withdrawn position against the reference fully inserted position. The calculated worth of the fully withdrawn rod is 2870 pcm.

Table 4-11. Stepped reactivity calculation of regulating rod.

% Withdrawn	k_{eff}	σ	IRW (pcm)
0%	0.96905	0.00016	0
5%	0.96974	0.00035	73
15%	0.97166	0.00033	277
25%	0.97328	0.00034	448
40%	0.97839	0.00034	985
50%	0.98298	0.00030	1462
60%	0.98688	0.00029	1864
75%	0.99169	0.00037	2356
85%	0.99466	0.00034	2657
95%	0.99634	0.00029	2827
100%	0.99677	0.00032	2870

A curve of the intgral regulating rod worth is given in Figure 4-13 in pcm from 0 to 100% withdrawn. The total worth of the rod is represented by the pcm value at 100% withdrawn. This curve shows that the worth curve is steepest near the axial center of the control rod, signifying the differential worth is greatest there. Consistently, the worth is less at the top and bottom of the rod as expected, signified by a flatter curve.

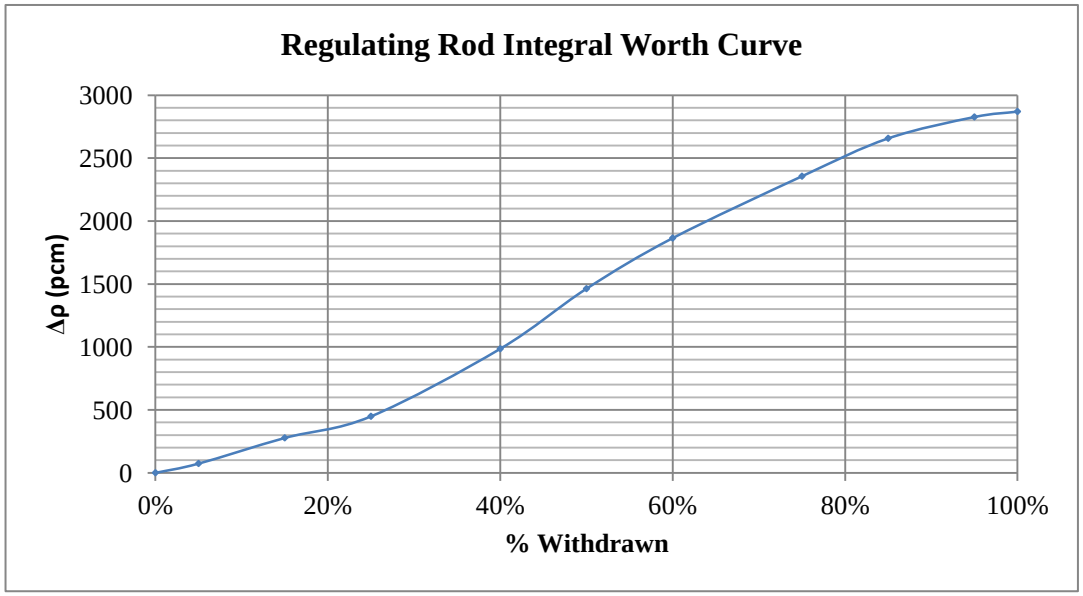

Figure 4-13. Calculated integral worth of regulating rod ($\sigma \leq 40$ pcm).

In Table 4-12 k_{eff} of the core with the safety rod withdrawn incrementally is given with the standard deviation. Additionally, the worth of the rod is given from the incrementally withdrawn position against the reference fully inserted position. The calculated worth of the fully withdrawn rod is 2190 pcm.

Table 4-12. Stepped reactivity calculation of safety rod.

% Withdrawn	k_{eff}	σ	IRW (pcm)
0%	0.96905	0.00016	0
5%	0.96989	0.00028	89
15%	0.97061	0.00032	166
25%	0.97258	0.00029	375
40%	0.97630	0.00032	766
50%	0.97886	0.00031	1034
60%	0.98185	0.00030	1345
75%	0.98608	0.00032	1782
85%	0.98819	0.00035	1999
95%	0.98936	0.00031	2118
100%	0.99006	0.00030	2190

A curve of the intgral safety rod worth is given in Figure 4-14 in pcm from 0 to 100% withdrawn. The total worth of the rod is represented by the pcm value at 100% withdrawn. This curve shows that the worth curve is steepest near the axial center of the control rod, signifying the differential worth is greatest there. Consistently, the worth is less at the top and bottom of the rod as expected, signified by a flatter curve.

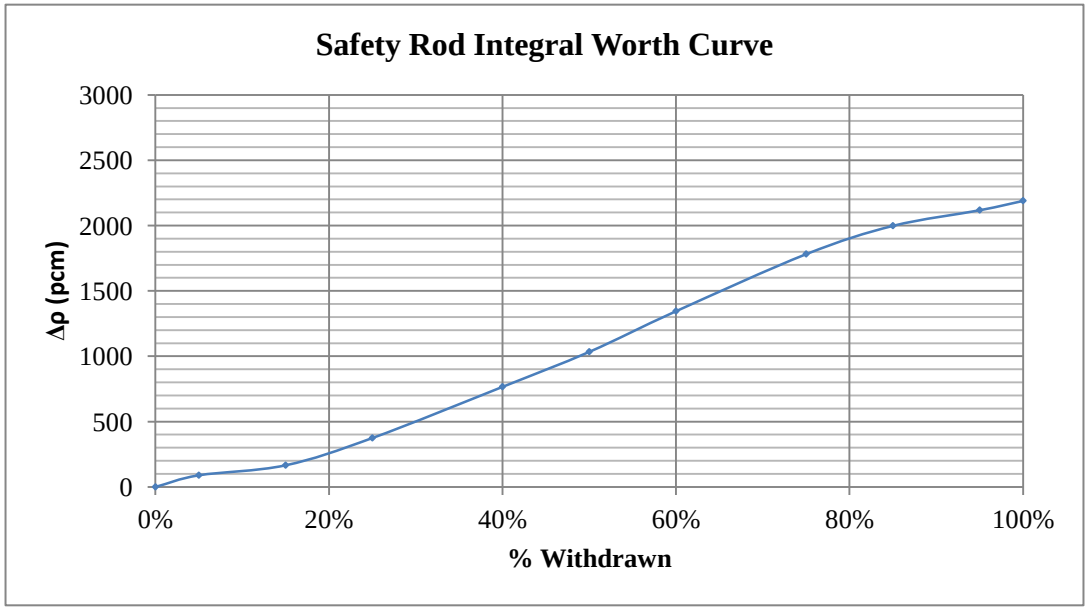

Figure 4-14. Calculated integral worth of safety rod (σ ≤ 40 pcm).

In Table 4-13 k_{eff} of the core with the shim rod withdrawn incrementally is given with the standard deviation. Additionally, the worth of the rod is given from the incrementally withdrawn position against the reference fully inserted position. The calculated worth of the fully withdrawn rod is 2432 pcm.

Table 4-13. Stepped reactivity calculation of shim rod.

% Withdrawn	k_{eff}	σ	IRW (pcm)
0%	0.96905	0.00016	0
5%	0.96909	0.00032	4
15%	0.97137	0.00032	246
25%	0.97247	0.00031	363
40%	0.97716	0.00031	856
50%	0.98176	0.00033	1336
60%	0.98407	0.00038	1575
75%	0.98819	0.00032	1999
85%	0.99095	0.00027	2281
95%	0.99186	0.00030	2373
100%	0.99244	0.00032	2432

A curve of the intgral shim rod worth is given in Figure 4-15 in pcm from 0 to 100% withdrawn. The total worth of the rod is represented by the pcm value at 100% withdrawn. This curve shows that the worth curve is steepest near the axial center of the control rod, signifying the differential worth is greatest there. Consistently, the worth is less at the top and bottom of the rod as expected, signified by a flatter curve.

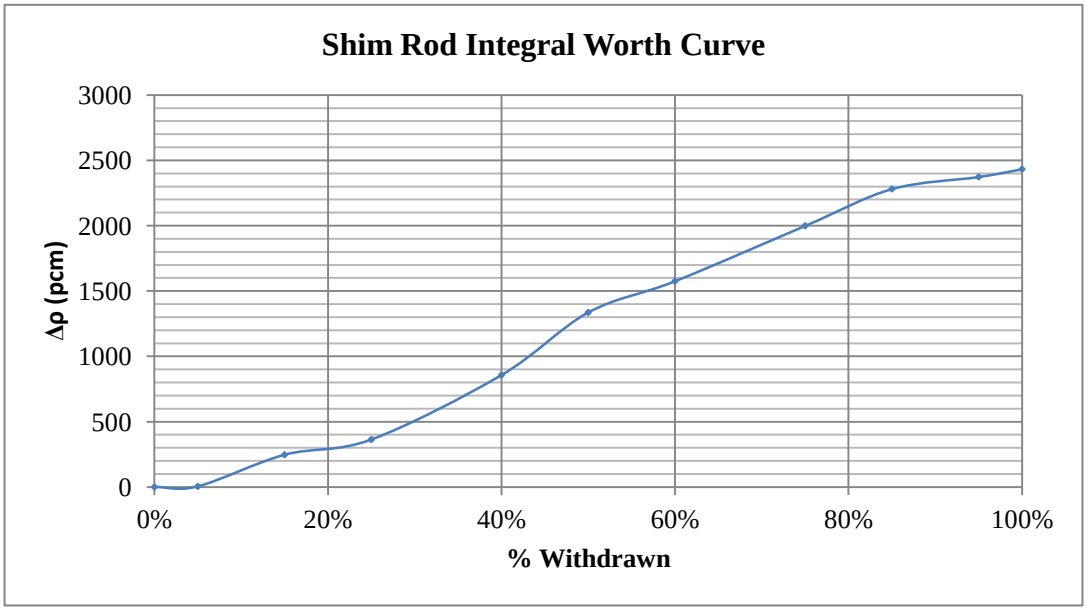

Figure 4-15. Calculated integral worth of shim rod (σ ≤ 40 pcm).

In Table 4-14 k_{eff} of the core with the transient rod withdrawn incrementally is given with the standard deviation. Additionally, the worth of the rod is given from the incrementally withdrawn position against the reference fully inserted position. The calculated worth of the fully withdrawn rod is 2433 pcm.

Table 4-14. Stepped reactivity calculation of transient rod.

% Withdrawn	k_{eff}	σ	IRW (pcm)
0%	0.96905	0.00016	0
5%	0.96987	0.00032	87
15%	0.96988	0.00029	88
25%	0.97337	0.00031	458
40%	0.97702	0.00032	842
50%	0.98065	0.00032	1221
60%	0.98374	0.00033	1541
75%	0.98885	0.00035	2066
85%	0.99035	0.00033	2219
95%	0.99228	0.00032	2416
100%	0.99245	0.00034	2433

A curve of the intgral transient rod worth is given in Figure 4-16 in pcm from 0 to 100% withdrawn. This curve shows that the worth curve is

steepest near the axial center of the control rod, signifying the differential worth is greatest there. Consistently, the worth is less at the top and bottom of the rod as expected, signified by a flatter curve.

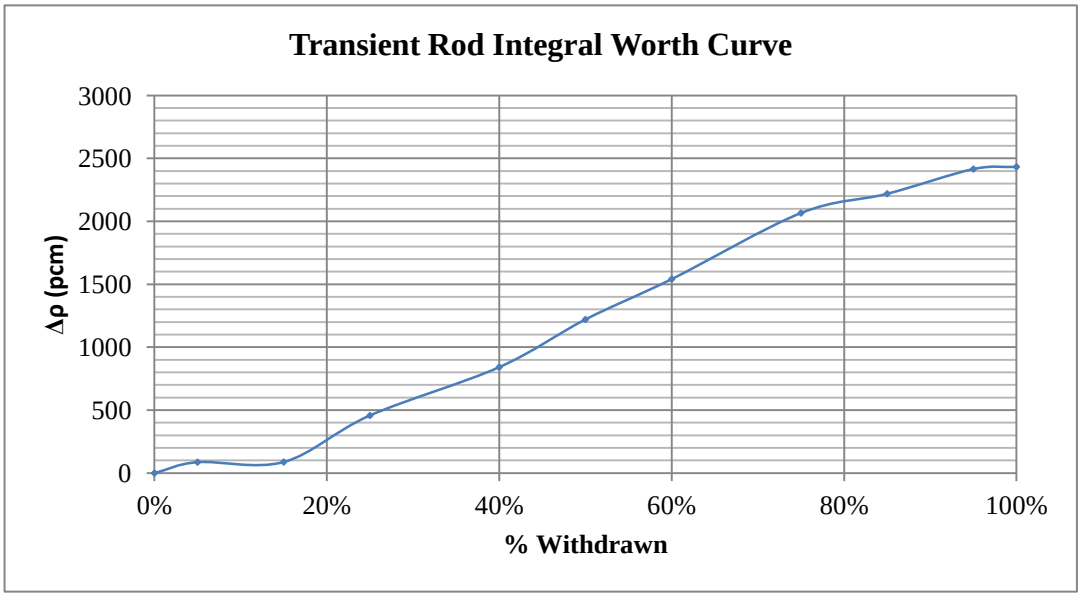

Figure 4-16. Calculated integral worth of transient rod (σ ≤ 40 pcm).

4.2.3.1. Measured Control Rod Worth

During post-conversion startup, the incremental control rod worth was measured using the period method. To start, the core was operating at steady state with the control rods at critical heights. Beginning from the fully inserted position, the control rod in question is withdrawn from the core a small amount (usually around 15-20%), and this increases the reactor power. After a short amount of time, delayed neutrons are not significantly contributing to the power increase and so the power can be characterized by a steady increase called the reactor period, which is defined as the amount of time required for power to increase by a factor of e. Following this characterization, a different control rod is fully inserted to keep the reactor from being supercritical. From the reactor period, the reactivity insertion can be determined, and the worth associated with the portion of the control rod that was removed can be determined. The control rod is continuously

removed in small increments until it is fully withdrawn from the core. Then a curve can be produced that gives the total worth of the segments of the control rod.

Table 4-15. Reactor period for rod pull measurement of integral rod worth.

Configuration	Pull Height	Period (s)	DRW (pcm/pull)	IRW (pcm)
Regulating Rod	0.0%	-	-	0.0
15	19.2%	8.922	441.1	441.1
16	29.8%	7.995	460.8	901.9
17	38.8%	7.725	466.9	1368.7
18	47.3%	7.876	463.5	1832.2
19	56.3%	7.860	463.8	2296.0
20	66.0%	9.424	431.1	2727.1
21	77.8%	10.634	408.8	3135.8
Safety Rod	0.0%	-	-	0.0
22	22.8%	10.245	415.7	415.7
23	34.8%	10.208	416.4	832.0
24	45.4%	10.926	403.7	1235.7
25	56.2%	10.658	408.3	1644.1
26	70.0%	9.263	434.2	2078.3
27	100.0%	10.669	408.2	2486.5
Shim Rod	0.0%	-	-	0.0
28	23.0%	9.213	435.2	435.2
29	35.0%	9.817	423.6	858.8
30	45.6%	9.669	426.4	1285.2
31	56.4%	10.050	419.2	1704.4
32	68.7%	10.702	407.6	2112.0
33	100.0%	7.441	473.4	2585.4
Transient Rod	0.0%	-	-	0.0
34	22.4%	9.160	436.3	436.3
35	33.8%	10.638	408.7	845.0
36	44.1%	9.634	427.0	1272.0
37	55.0%	9.474	430.1	1702.1
38	67.2%	10.608	409.2	2111.3
39	80.9%	15.545	337.8	2449.1
40	100.0%	37.274	191.0	2640.1

This procedure is repeated for each control rod and the worth of each rod is measured during startup.

In Table 4-15, each configuration corresponds to the similarly numbered configuration in Table 4-10. Table 4-10 gives the critical rod heights for every control rod for steady-state, low power operation in between control rod pulls. Table 4-15 gives the percentage a rod was pulled following the establishment of steady-state operation, and gives the associated reactor period recorded in the startup logs. From the reactor period, and using the methodology described in §3.4.6, the differential and integral rod worths measured during startup can be plotted and compared to values predicted by the MCNP model.

Each control rod pull described previously and measured using the reactor period method can also be modeled using MCNP. From the critical configuration, the pulled rod will result in a configuration that is slightly above critical. The difference in k_{eff} between the critical configuration and the calculation with the control rod pulled can be used to determine what the model estimates the incremental portion of that rod to be worth. The results of this calculation are presented in Table 4-16.

Table 4-16. k_{eff} for rod pull measurement of integral rod worth.

Configuration	Critical k_{eff}	Pull Height	Pull k_{eff}	DRW (pcm/pull)	IRW (pcm)
Regulating Rod	1.00485	0.0%	-	0.0	0.0
	1.00381	19.2%	1.00729	241.1	241.1
	1.00341	29.8%	1.00701	316.6	557.6
	1.00349	38.8%	1.00683	338.5	896.2
	1.00292	47.3%	1.00582	230.8	1127.0
	1.00289	56.3%	1.00653	357.6	1484.6
	1.00247	66.0%	1.00590	298.4	1783.0
	1.00520	77.8%	1.00653	402.4	2185.4
	-	100.0%	1.00719	196.6	2381.9
Safety Rod	1.00392	0.0%	-	0.0	0.0
	1.00410	22.8%	1.00655	260.3	260.3
	1.00326	34.8%	1.00601	189.1	449.4
	1.00281	45.4%	1.00618	289.3	738.6
	1.00279	56.2%	1.00573	289.5	1028.1
	1.00392	70.0%	1.00638	355.7	1383.9
	-	100.0%	1.00642	247.4	1631.3
Shim Rod	1.00262	0.0%	-	0.0	0.0
	1.00357	23.0%	1.00617	351.9	351.9
	1.00265	35.0%	1.00594	234.8	586.7
	1.00294	45.6%	1.00653	384.5	971.1
	1.00343	56.4%	1.00634	336.9	1308.0
	1.00412	68.7%	1.00662	315.8	1623.8
	-	100.0%	1.00824	407.0	2030.8
Transient Rod	1.00406	0.0%	-	0.0	0.0
	1.00300	22.4%	1.00543	135.7	135.7
	1.00237	33.8%	1.00524	222.2	357.9
	1.00362	44.1%	1.00554	314.5	672.4
	1.00349	55.0%	1.00669	303.9	976.2
	1.00454	67.2%	1.00657	304.9	1281.2
	1.00490	80.9%	1.00714	257.0	1538.2
	-	100.0%	1.00664	172.0	1710.2

In Figure 4-17, the curve of the calculated integral worth of the regulating rod (determined by calculating the excess from each rod pull, Table 4-16) is plotted against the measured integral worth of the regulating rod (determined from the reactor period after each pull, Table 4-15), and against the

predicted worth (calculated with MCNP, Table 4-11 through Table 4-14). The worth measured directly from the period method is largest; while the worth calculated by MCNP from each rod pull results in the lowest worth. The shapes of the integral worth curves show the expected sigmoid shape, but the total worth represented by each method varies greatly, especially toward the end of the rod.

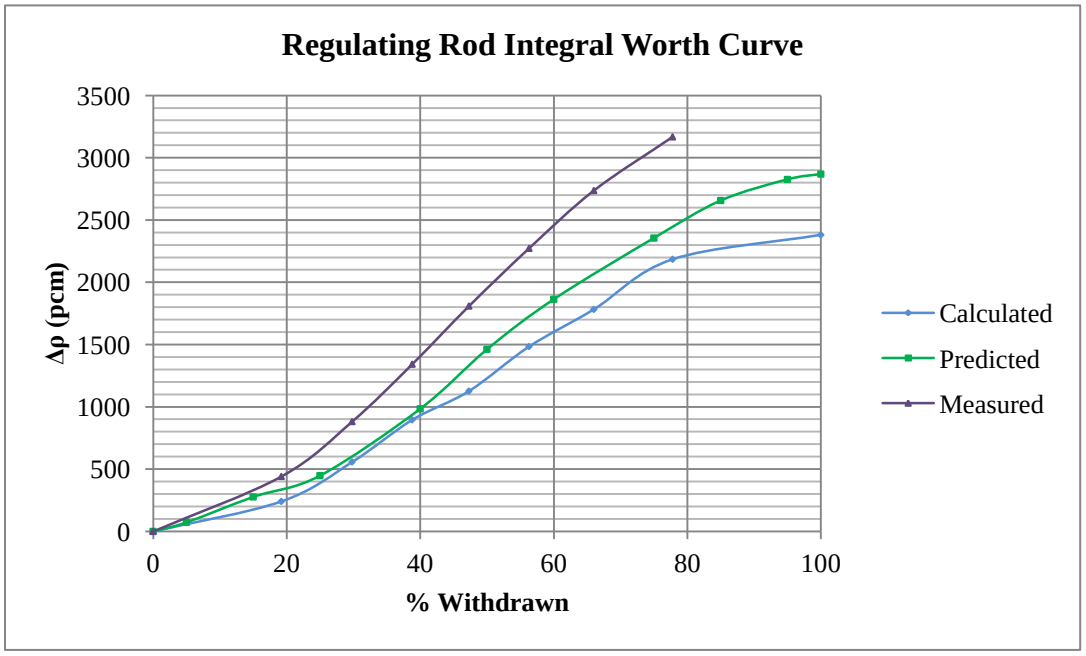

Figure 4-17. Measured integral worth of regulating rod.

In Figure 4-18, the curve of the calculated integral worth of the regulating rod (determined by calculating the excess from each rod pull, Table 4-16) is plotted against the measured integral worth of the regulating rod (determined from the reactor period after each pull, Table 4-15), and against the predicted worth (calculated with MCNP, Table 4-11 through Table 4-14). The worth measured directly from the period method is largest; while the worth calculated by MCNP from each rod pull results in the lowest worth. The shapes of the integral worth curves show the expected sigmoid shape, but the total

worth represented by each method varies increasingly as the rod is removed further.

Figure 4-18. Measured integral worth of safety rod.

In Figure 4-19, the curve of the calculated integral worth of the regulating rod (determined by calculating the excess from each rod pull, Table 4-16) is plotted against the measured integral worth of the regulating rod (determined from the reactor period after each pull, Table 4-15), and against the predicted worth (calculated with MCNP, Table 4-11 through Table 4-14). The worth measured directly from the period method is largest; while the worth calculated by MCNP from each rod pull results in the lowest worth. The shapes of the integral worth curves show the expected sigmoid shape, and the total worth represented by each method varies slightly, increasing more in the second half of the rod.

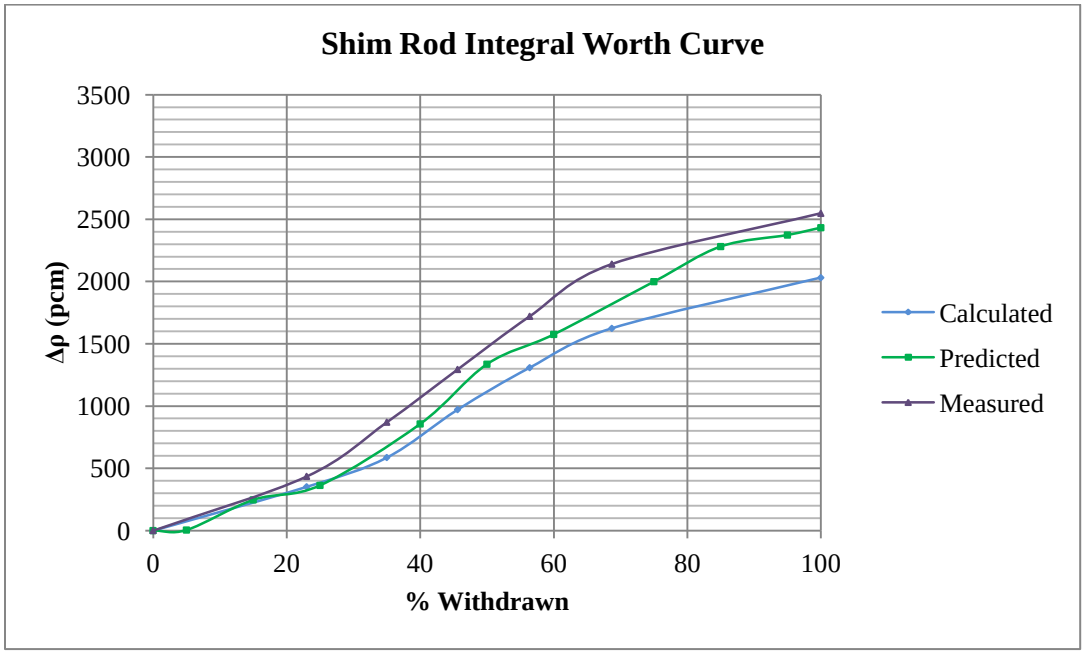

Figure 4-19. Measured integral worth of shim rod.

In Figure 4-20, the curve of the calculated integral worth of the regulating rod (determined by calculating the excess from each rod pull, Table 4-16) is plotted against the measured integral worth of the regulating rod (determined from the reactor period after each pull, Table 4-15), and against the predicted worth (calculated with MCNP, Table 4-11 through Table 4-14). The worth measured directly from the period method is largest; while the worth calculated by MCNP from each rod pull results in the lowest worth. The shapes of the integral worth curves show the expected sigmoid shape, but the total worth represented by each method varies greatly, especially as the rod is removed further.

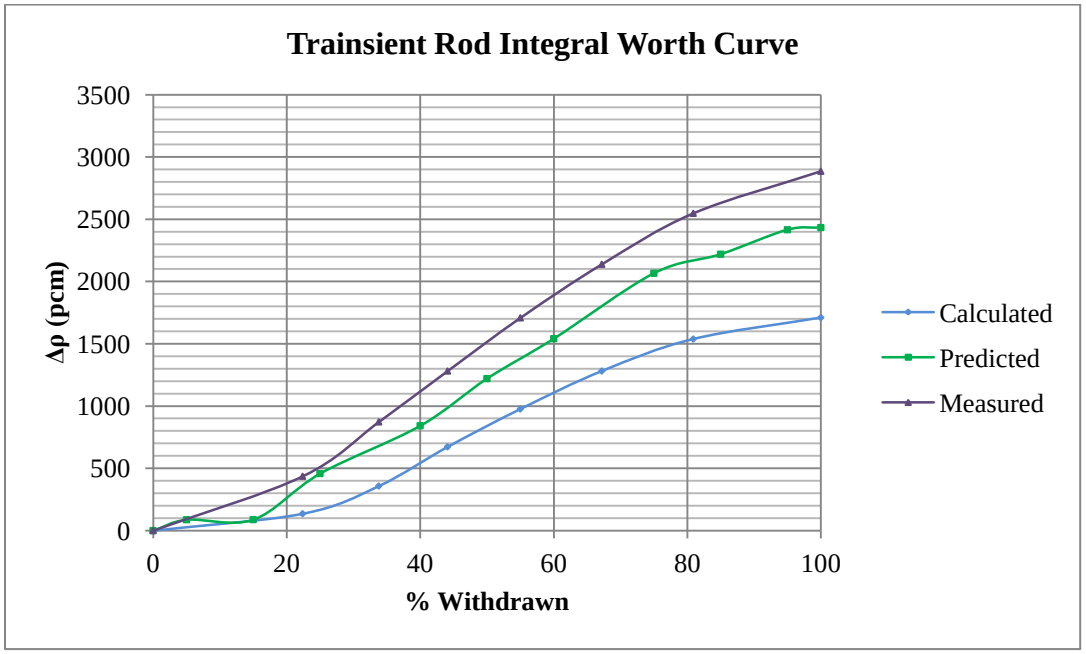

Figure 4-20. Measured integral worth of transient rod.

Perfect agreement between the measured and calculated control rod worth curves is not expected for a few reasons. First, determining control rod worth from the period can be inaccurate due to the method of estimating the reactor period. Determining when it seems transients have died out and deciding that power is changing at a constant pace leaves a lot up to the interpretation of the measurer. While in reality this may produce reliable results, they will not have the same integrity as an exact MCNP calculation.

A second reason we do not expect the results to align perfectly is that the control rods were in different configurations for each set of measurements. For the calculated integral control rod worth, all control rods were fully inserted except the rod in question, which was incrementally being withdrawn. For all of these calculations, the MCNP model showed the reactor in a subcritical state. For the period method, the reactor began in a critical configuration, then control rods were removed in part from the core. Each maneuver resulted in a supercritical core. Changes that occur in a core with excess reactivity will effectively have greater reactivity impacts than in

a core that is subcritical. This is consistent with the findings presented in this section, as the period measurement method tends to produce integral rod worth curves that have slightly more worth than the calculated curves.

Finally, a source of inaccuracy in both curves lies in the fact that the differential worth of each step is attributed to the top of the step, rather than somewhere closer to the middle of the step. This results in an underestimation of the true integral worth of the control rod. Differential calculations taken in finer step sizes would produce a truer curve, but it is not practical to perform so many calculations, or to make very small pulls of the control rods (due to excessively long reactor periods associated with small changes in reactivity). Furthermore, the error of each pull is cumulative, so more pulls (and hence more error), may invalidate any benefit derived from finer step sizes for differential worth calculations.

5. Conclusions

The general trends of the calculations performed and presented in the previous chapter characterize potential sources of unnecessary model bias. The addition of beam ports 1 and 2 gave a 164 pcm decrease in results, 30% water saturation of the radial reflector resulted in an additional 453.8 pcm decrease, as-built fuel compositions resulted in a 894.3 pcm increase, changes to the neutron data library resulted in a 69.5 pcm decrease, and sensitivities in the hafnium concentration had negligible effects. The net result in these changes was a 207.0 pcm increase in k_{eff}. The systematic changes have fine-tuned the model to be a more accurate depiction of the actual post-conversion, LEU OSTR core. The overarching impact of the calculations considered in this work will be the inclusion of changes in the model in such a way that the reactivity bias is reduced as much as possible.

Consistent, precise results of benchmarking calculations lend to the determination of a fixed reactivity bias that may be assumed an inherent feature of the OSTR until determined otherwise. This bias and associated error may be used as a correction factor to calculations based on this core. The first 13 low-power critical configurations result in a k_{eff} of 1.00205, equivalent to a \$0.273 bias. With consideration for all critical configurations during control rod worth measurements, the first 41 low-power critical configurations result in a k_{eff} of 1.00304, equivalent to a \$0.405 bias. The consistency in the results demonstrates fidelity in the calculation. This bias can be applied, with standard error, to other calculations performed using the model developed as a part of this work to correct the slight over-estimation of k_{eff}.

These results are limited. They only consider the core immediately following the conversion to fresh unirradiated fuel. All of the measurements were conducted at low power levels and temperatures. As the fuel is burned even for short amounts of time, isotopic concentrations begin to change. Many isotopes with strong negative impact on reactivity such as fission product poisons with be produced, and the concentration of fissile isotopes will increase. Higher fuel and coolant temperatures

are associated with higher power levels, and reactivity coefficients will begin to take greater effect on the reactivity of the system.

5.1. Uncertainties

Uncertainties and error are possible in a number of different forms due to the nature of these calculations. They range from uncertainties in measurements of material concentrations or geometries, the proper transcription and manipulation of the data, correctly and completely making changes to the MCNP input, and extraction and use of the data.

The most significant result of this work is the ability to determine a bias in the model, if one can be determined at all, and the magnitude of that bias. This relies heavily on measured critical core configurations that occurred during low power startup testing, and the ability of the MCNP model to accurately model a critical core. The control rods movements are only measured in 0.1% increments of their total height. Inaccurate readings or control rod positions that are fairly close but not exactly matching the heights recorded and modeled can lead to large variations in the calculated k_{eff} for any critical configuration. Although a standard deviation is given to the Monte Carlo determination of k_{eff}, additional uncertainties should be developed to quantify and bound the error that may exist in the determination of k_{eff} for critical core configurations.

5.2. Future Work

It was seen previously that calculations at higher power levels resulted in greater predicted k_{eff} values, and the critical configuration modeled in this case was not included in the results of the low power critical configuration calculations. In the future, other low power configurations could be used to aid in informing the size of the calculation bias if the size of the reactivity contribution by the increase in power were incorporated. The theoretical power defect could be estimated from the MCNP model, then applied to critical configurations that occur at higher power levels in order to increase the number of data points used in the determination of the model bias.

Although various combinations of cross section libraries were explored, this consideration is not fully vetted. As a review of the literature suggested, less recent versions of ENDF data libraries may contain more accurate cross section data for zirconium, so rather than using the current ENDF/B-VII library, ENDF/B-VI was used for all zirconium materials instead. Calculations were consistent with this trend, and implementation of this change did in fact produce the most agreeable results, reducing the margin between measured and calculated values of k_{eff} by the most. The differences between sets of data for this material should be explored more and better understood. This way an informed decision can be made as to what cross section library should be used.

Much of the data used in the updates made to the MCNP model have an uncertainty attached to them. While some variables were perturbed to understand the general effects they had on calculations, if they had any effect at all, not all variables were considered. It may be useful to perturb a larger list of variables. Testing the sensitivity of many more parameters within their range of uncertainty or measurement tolerances may provide greater insight into additional contributors to the calculation bias.

6. Bibliography

[1] Oregon State University. *Safety Analysis Report for the Conversion of the Oregon State TRIGA® Reactor from HEU to LEU Fuel.* November, 2007.

[2] U.S. Nuclear Regulatory Commission. *10 CFR 50.64: Limitations on the use of highly enriched uranium (HEU) in domestic non-power reactors, 1986.* NRC Regulations.

[3] General Atomics. "TRIGA Reactors United States." http://www.ga-esi.com/triga/about/install_usa.pdf. February 2003.

[4] Keller, S. Todd. "Oregon State University TRIGA Reactor Post Conversion Reactor Startup Report." *U.S. Nuclear Regulatory Commission* 50-243 (2009): 1-72.

[5] Keller, S. Todd, and Steven R. Reese. "Going from HEU to LEU: Conversion of the Oregon State TRIGA Reactor." *31st International Meeting on Reduced Enrichment for Research and Test Reactors* 1 (2009): 1-11.

[6] Perez, Pedro, John Bernard, Leo M. Bobek, William G. Vernetson. "University Research Reactors: A Brief Overview." National Organization of Test, Research, and Training Reactors. September 2000.

[7] Bess, John, Thomas Maddock, and Margaret Marshall. *Fresh-Core Reload of the Neutron Radiography (NRAD) Reactor with Uranium(20)-Erbium-Zirconium-Hydride Fuel, DRAFT*. Idaho Falls: Idaho National Laboratory, 2012.

[8] RSICC. MCNP5 Manual.

[9] Radiation Center, Oregon State University. OSTR Startup Logs. October 2008.

[10] Chart of the Nuclides, 16th Edition.

[11] Bess, John D., Lee M. Montierth. "Neutronic Simulation of NRAD Reactor JEU Conversion Start-Up Tests." TRTR/IGORR 2010 Joint Meeting. September 2010.

[12] Los Alamos National Laboratory. MCNP Users Manual.

[13] Perry, Robert H., Don W. Green, and James O. Maloney. "Physical Properties

of Sorbent Materials." In *Perry's Chemical engineers' handbook*. 6th ed. New York: McGraw-Hill, 1984. 16-9.

[14] Podesta, Michael. "Solids: Comparison with Experiment." In *Understanding the properties of matter*. 2nd ed. London: Taylor & Francis, 2001. 178.

[15] Oregon State University. *Control Rod Calibration by the Period and Rod Drop Methods.* Laboratory Write-Up, NE 457/557. 2011.

Additional References

[16] Argonne National Laboratory. *Examples of LEU Conversion Analyses in the RERTR Program.* http://www.rertr.anl.gov/LEUCONV.html. July 2008.

[17] Borio di Tigliole, A., A. Cammi, M. Clemenza, V. Memoli, L. Pattavina, and E. Previtali. "Benchmark evaluation of reactor critical experiments and neutron fluxes distributions at zero power for the TRIGA Mark II reactor of the University of Pavia using the Monte Carlo code MCNP." *Progress in Nuclear Energy* 52 (2010): 494-502.

[18] Candalino, Robert. *Engineering Analysis of Low Enriched Uranium Fuel Using Improved Zirconium Hydride Cross Sections*. Texas: Texas A&M University, 2006. Thesis.

[19] Dodd, B., A.C. Klein, B.R. Lewis, and P.A. Merritt. "Results of the MCNP Analysis of 20/20 LEU Fuel for the Oregon State University TRIGA Reactor." *14th TRIGA Users Conference* 1 (1995): 1-14.

[20] Huda, M.Q.. "Computational analysis of Bangladesh 3 MW TRIGA research reactor using MCNP4C, JENDL-3.3 and ENDF/B-VI data libraries." *Annals of Nuclear Energy* 33 (2006): 1072-1078.

[21] Keller, S. Todd. "Modeling the Oregon State University TRIGA Reactor Using the Atilla Three-Dimensional Deterministic Transport Code." *2007 TRTR Conference* 1 (2007): 1-25. Presentation.

[22] Keller, S. Todd. *Modeling the Oregon State University TRIGA Reactor Using the Atilla Three-Dimensional Deterministic Transport Code*. Corvallis: Oregon

State University, 2007. Thesis.

[23] Keller, S. Todd, and Steven R. Reese. "Going from HEU to LEU: Conversion of the Oregon State TRIGA Reactor." *Proceedings of the Institute of Nuclear Materials Management Annual Meeting* 1 (2009): 1-10.

[24] Khan, R., S. Karimzadeh, H. Bock, and M. Villa. "Modeling a TRIGA Mark II Biological Shield using MCNP5." *Nuclear Energy for New Europe* 1 (2009): 1-8.

[25] Khan, R., M. Villa, and H. Bock. "Monte Carlo Modelling of Void Coefficient of Reactivity Experiment." *Research Reactor Fuel Management Conference* 1 (2010): 1-6.

[26] Marcum, Wade R., and Brian G. Woods. "Thermal Hydraulic Analysis for the Oregon State Reactor Using RELAP5-3D." *TRTR Conference* 1 (2007): 1-25. Presentation.

[27] Marcum, Wade R.. *Thermal Hydraulic Analysis of the Oregon State TRIGA Reactor Using RELAP5-3D*. Corvallis: Oregon State University, 2008. Thesis.

[28] Merritt, Patrick A. *MCNP Benchmarking and Analysis of Oregon State University TRIGA Reactor*. Corvallis: Oregon State University, 1999.

[29] Reese, Steve. "Oregon State University Response to RAI Regarding Conversion Amendment." *U.S. Nuclear Regulatory Commission* 50-243 (2008): 1-117.

[30] Snoj, Luka, and Matjaz Ravnik. "Calculation of Power Density with MCNP in TRIGA Reactor." *Nuclear Energy for New Europe* 1 (2006): 1-6.

[31] Stevens, John G. "Core Modifications to address technical challenges of conversion." *Russian-American Symposium on the Conversion of Research Reactors to Low Enriched Fuel* 1 (2011): 1-18.

[32] Uddin, M.N., M.M. Sarker, M.J.H. Khan, and S.M.A. Islam. "Computational analysis of neutronic parameters for TRIGA Mark-II research reactor using evaluated nuclear data libraries." *Annals of Nuclear Energy* 37 (2010): 302-309.